Title: All-optical closed-loop voltage clamp for precise control of muscles and neurons in live animals

Authors: Amelie C.F. Bergs[1,2], Jana F. Liewald[1,2], Silvia Rodriguez-Rozada[3], Qiang Liu[4, 5], Christin Wirt[1,2], Artur Bessel[6], Nadja Zeitzschel[1,2], Hilal Durmaz[1,2], Adrianna Nozownik[3], Johannes Vierock[7], Cornelia I. Bargmann[4,8], Peter Hegemann[7], J. Simon Wiegert[3], Alexander Gottschalk[1,2,*]

Affiliations:

[1] Buchmann Institute for Molecular Life Sciences, Goethe University; Max-von-Laue-Strasse 15, D-60438 Frankfurt, Germany.

[2] Institute of Biophysical Chemistry, Goethe University; Max-von-Laue-Strasse 9, D-60438 Frankfurt, Germany.

[3] Research Group Synaptic Wiring and Information Processing, Center for Molecular Neurobiology Hamburg, University Medical Center Hamburg-Eppendorf, D-20251 Hamburg, Germany.

[4] Lulu and Anthony Wang Laboratory of Neural Circuits and Behavior, The Rockefeller University, New York, NY 10065, USA.

[5] Department of Neuroscience, City University of Hong Kong, Tat Chee Avenue, Kowloon Tong, Hong Kong, China.

[6] independent researcher: Melatener Strasse 93, D-52074 Aachen, Germany.

[7] Institute for Biology, Experimental Biophysics, Humboldt University, D-10115 Berlin, Germany.

[8] Chan Zuckerberg Initiative, Palo Alto, USA.

* Corresponding author. Email: a.gottschalk@em.uni-frankfurt.de

Abstract: Optogenetics are used to stimulate or inhibit neurons. Because optogenetic stimulation is typically static, neurons and circuits can quickly adapt, allowing perturbation, but not true control. To overcome this, we established an optogenetic voltage-clamp (OVC). The genetically encoded voltage-indicator QuasAr2 provides information for fast, closed-loop optical feedback to the bidirectional optogenetic actuator BiPOLES. Voltage-dependent fluorescence is held within tight margins, thus clamping the cell at a distinct potential. We established the OVC in muscles and neurons of *Caenorhabditis elegans*, and transferred it to hippocampal neurons in rat brain slices. We calibrated fluorescence signals to electrically measured membrane potentials, showed that the OVC reports on homeostatically altered cellular physiology in mutants affecting neurotransmission, and that it can dynamically clamp spiking. The OVC combines non-invasive imaging with the control capabilities of electrophysiology. Its applicability to individual cells facilitates high-throughput contact-less electrophysiology and paves the way for true optogenetic control in behaving animals.

One-Sentence Summary: Next generation optogenetic control of neuron function *via* optical feedback for non-invasive substitution of electrophysiology.

Introduction

Identifying connections between distinct neurons, and their contribution to driving behavior, is a central issue in neuroscience [1, 2]. To explore such relations, methods to record and concurrently regulate neural activity are needed [3]. Also, high-throughput screening approaches in excitable cell physiology require the use of such methods. To date, diverse approaches to control or observe excitable cell function are used. Patch-clamp electrophysiology provides superior temporal accuracy and sensitivity, yet is limited by its invasiveness [4-6]. Ca^{2+} imaging, applicable in intact living organisms, enables integrating cell physiology and behavioral output [7-9]. However, due to sensor Ca^{2+} buffering and the weak, non-linear correlation of cytosolic Ca^{2+} concentration and membrane voltage, this technique suffers from comparably low temporal resolution, and fails to resolve subthreshold voltage transients or high-frequency action potentials (APs). Further, as it does not directly measure membrane voltage and since Ca^{2+} concentration does not fall below basal cytosolic levels, Ca^{2+} imaging is unsuited to reveal synaptic inhibition. This is offered by genetically encoded (fluorescent) voltage indicators (GEVIs), e.g. rhodopsin-based GEVIs, among others [10-17]. The fluorescence of retinal, embedded in rhodopsins, reliably monitors voltage dynamics at millisecond time scales. Since rhodopsin-based GEVIs emit near-infrared light, they can be multiplexed with optogenetic actuators of membrane currents, to selectively photostimulate or -inhibit activity of excitable cells with high spatiotemporal precision [18-20]. Single optogenetic actuators were employed together with imaging tools, which allows to unidirectionally perturb and observe, but not to fully control activity within a neural circuit [11, 12, 21]. This approach was implemented as “(i)-Optopatch”, comprising the voltage indicator QuasAr2 and the blue-light activated Channelrhodopsin (ChR) CheRiff [11, 12]. Bidirectional optical modulation and readout of voltage was implemented as light-induced electrophysiology (LiEp) for drug screening, however, this approach lacked a feedback loop [22]. A bidirectional approach, using ChR2 and halorhodopsin (NpHR) as actuation pair with feedback control – “optoclamp” – employed extracellular microelectrode arrays instead of GEVIs [23]. This approach observes (and clamps) neuronal ensembles and their average firing rates, but not single neurons, by indirect voltage readout.

True all-optical control over excitable cell activity with closed-loop feedback, as in voltage-clamp electrophysiology, should combine two opposing optogenetic actuators for de- and hyperpolarization, as well as a GEVI. Such a system could respond to intrinsic changes in membrane potential. It would also prevent inconsistent activity levels arising from cell-to-cell variation in optogenetic tool expression levels, not taken into account when static stimulation

patterns are used. The system should synergize the non-invasive character of imaging methods with the control capabilities of electrophysiology.

Here, we established an optogenetic voltage-clamp (OVC) in *Caenorhabditis elegans* and rat hippocampal organotypic slices. The OVC uses QuasAr2 for voltage read-out [11, 20], and BiPOLES, a tandem protein comprising the depolarizer Chrimson and the hyperpolarizer *Gt*ACR2, stimulated by orange and blue light, respectively, for actuation [19, 24-27]. Spectral separation and balanced 1:1 expression of BiPOLES enable gradual transitions from depolarized to hyperpolarized states, and *vice versa*. QuasAr2 fluorescence is used to compute a feedback of color-adapted light signals transmitted to BiPOLES, in closed-loop at 90 Hz, thus keeping the voltage-dependent fluorescence at a desired level. We characterized the system in body-wall muscle cells (BWMs), as well as in cholinergic and GABAergic motor neurons. Simultaneous measurements allowed calibrating fluorescent signals to actual membrane voltages. In *unc-13* mutants, the OVC readily detected altered excitability of muscle, as a response to the reduced presynaptic input. In rodent neurons, the OVC also modulated fluorescence and voltage, yet with a smaller range and acting more as a conductance-clamp, due to the resting potential being close to Cl^- reversal potential. Last, in spontaneously active tissues, i.e., pharyngeal muscle and the motor neuron DVB [28-31], the OVC could dynamically follow and counteract native APs.

Results

Reading GEVI fluorescence to steer optogenetic actuators with light feedback in closed-loop

An OVC should measure voltage-dependent fluorescence of an excitable cell, e.g. *via* a rhodopsin-GEVI [10, 11], and provide adjusted light-feedback to optogenetic actuators of membrane voltage, e.g. cation- and anion-selective rhodopsin channels [19, 27, 32, 33] (**Fig. 1A**). The OVC needs to work in closed-loop, to quickly counteract intrinsic activity. We first implemented suitable hard- and software (**Fig. 1B**): To excite fluorescence of rhodopsin GEVIs (e.g. QuasAr2, emitting in the far-red) [10, 11], we expanded a 637 nm laser to cover a larger field of view. GEVI fluorescence of a region of interest (ROI) was monitored by a sensitive camera, and compared to a target value (**Fig. 1C, Extended data Fig. 1A-C**). Light feedback is sent to the sample from a monochromator, whose wavelength limits (400-600 nm, near where the chosen hyperpolarizing and depolarizing optogenetic tools are maximally activated) could be accessed at 100 µs and 0.1 nm temporal and spectral resolution, respectively.

Communication between camera and monochromator is provided by a custom-written script in Beanshell (part of µManager interface [34]), processing incoming gray values into relative changes

of fluorescence ($\Delta F/F_0$) (**Fig. 1C, Extended data Fig. 1A-C**), and operating at ca. 90 fps speed (10 ms exposure). Since GEVIs exhibit photobleaching, $\Delta F/F_0$ values would gradually deviate from actual voltage levels. Thus, an initial calibration phase is used to calculate correction parameters (**Fig. Extended data Fig. 1D, E**). Once the system can access bleach-corrected $\Delta F/F_0$ values, it feeds them into a decision tree algorithm (**Fig. Extended data Fig. 1A**), where they are compared to a desired holding $\Delta F/F_0$ value. Deviation between target and actual $\Delta F/F_0$ determines the wavelength change of the monochromator (I(ntegral)-controller; **Extended data Fig. 1A**). An alternative algorithm, using a PID controller [35] and Kalman filter [36] for sensor smoothing, reduced the control deviation, but did not increase overall system performance (see methods; **Extended data Fig. 2**).

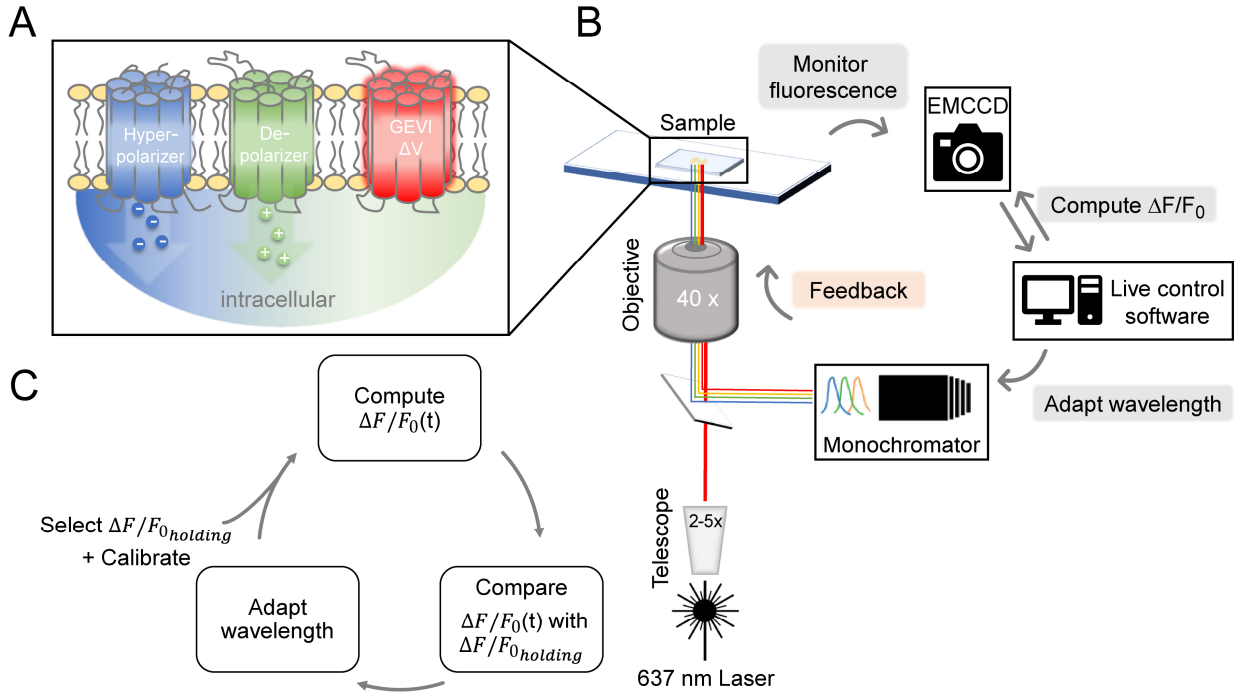

Fig. 1. Components, setup and functionality of the OVC. (A) Molecular OVC components: Two counteracting optogenetic actuators for de- and hyperpolarization, and a voltage indicator. **(B)** Hardware setup and communication: Membrane voltage is monitored via a fast and sensitive (sCMOS or EMCCD) camera; gray values are processed by live control software. Based on the difference to the set holding value, a feedback of light from a monochromator is sent to the optogenetic actuators. **(C)** OVC feedback mechanism: After selection of clamping parameters and calibration for bleaching correction, $\Delta F/F_0$ is calculated and compared with the set value, to adapt the wavelength accordingly, in closed-loop.

Combining single actuators with QuasAr2 for unidirectional steering of membrane voltage

First, we expressed QuasAr2 in *C. elegans* body wall muscles (BWMs). 20 s calibration under 637 nm laser light sufficed to estimate photobleaching parameters. 300 µW/mm^2 blue light or presenting the full spectrum (400 to 600 nm) caused no additional bleaching and did not affect

131 QuasAr2 fluorescence (**Extended data Fig. 1D-F**). Thus, monochromator light does not affect
132 bleaching-corrected fluorescence and estimated membrane voltages. To test the feedback loop,
133 we expressed either *Chlamydomonas reinhardtii* ChR2(H134R), or *Guillardia theta* anion
134 channelrhodopsin *Gt*ACR2, in cholinergic motor neurons (**Extended data Fig. 3A**), to manipulate
135 muscle voltage indirectly via light-induced (de-)activation of motor neurons (**Extended data Fig.**
136 **3B, C**). ChR2 or *Gt*ACR2 activation allowed adjusting QuasAr2 fluorescence to values between
137 +20 and -15 % $\Delta F/F_0$, respectively (**Extended data Fig. 3D**). However, fluorescence (i.e., voltage)
138 returned to baseline only by intrinsic membrane potential relaxation (**Extended data Fig. 3D-G**),
139 thus limiting temporal resolution: For ChR2, fluorescence reached the target range after 150 ±
140 12.7 ms and relaxed within 678 ± 148.9 ms (**Extended data Fig. 3G**; 254 ± 20.4 ms and 239.5 ±
141 29.9 ms, respectively, for *Gt*ACR2).

142 **BiPOLES enables bidirectional voltage-clamping in *C. elegans* muscle**

143 Optogenetic de- or hyperpolarization of cholinergic motor neurons affects muscle activation and
144 body contraction or elongation [32, 37]. We used this to assess combinations of spectrally distinct,
145 opposing actuator pairs, like ChR2 (470 nm) and *Gt*ACR1 (515 nm), or *Natronomonas pharaonis*
146 halorhodopsin NpHR (590 nm) (**Extended data Fig. 4A-D**). Yet, as separate expression
147 precluded control over relative expression levels, one actuator was typically outperformed by the
148 other, impeding precise control of membrane potential. To overcome this problem, we used the
149 tandem protein BiPOLES, in which the de- and hyperpolarizers Chrimson and GtACR2 (590 nm
150 and 470 nm, respectively) are linked as one sequence [26] (**Fig. 2A**).
151 BiPOLES activation with a 400-600 nm ramp evoked robust bidirectional effects on body length
152 (**Extended data Fig. 4E**). We thus co-expressed BiPOLES and QuasAr2 in BWMs (**Fig. 2A, B**).
153 BiPOLES expressed at comparably low levels, at the plasma membrane (PM) and in few
154 intracellular aggregates, while QuasAr2 localized mainly to the PM. QuasAr2 excitation (637 nm)
155 causes some activation of Chrimson (their spectra overlap [25, 38]; **Extended data Fig. 5A**). As
156 BiPOLES enables bidirectional voltage steering, we counteracted Chrimson currents by setting
157 the monochromator to a compensatory wavelength. This was adjusted until -5 and 5 % $\Delta F/F_0$
158 could each be maintained ≈5 s. In animals expressing the OVC in BWMs and/or cholinergic
159 neurons, 637 nm laser light caused reduced motor behavior, as this is sensitive to perturbation of
160 muscle and/or motor neuron function; however, adding compensation light (521 ± 1.68 nm)
161 restored body length, as well as swimming behavior, (**Extended data Fig. 5C-F, Extended data**
162 **video 1**). BWMs expressing the OVC showed voltage fluctuations comparable to animals
163 expressing QuasAr2 only (**Extended data Fig. 4F**). Also, despite 637 nm laser light, Chrimson

could be further activated by 590 nm (300 µW/mm²) light, causing a ca. 2.3 % $\Delta F/F_0$ increase of QuasAr2 fluorescence (**Extended data Fig. 5B**).

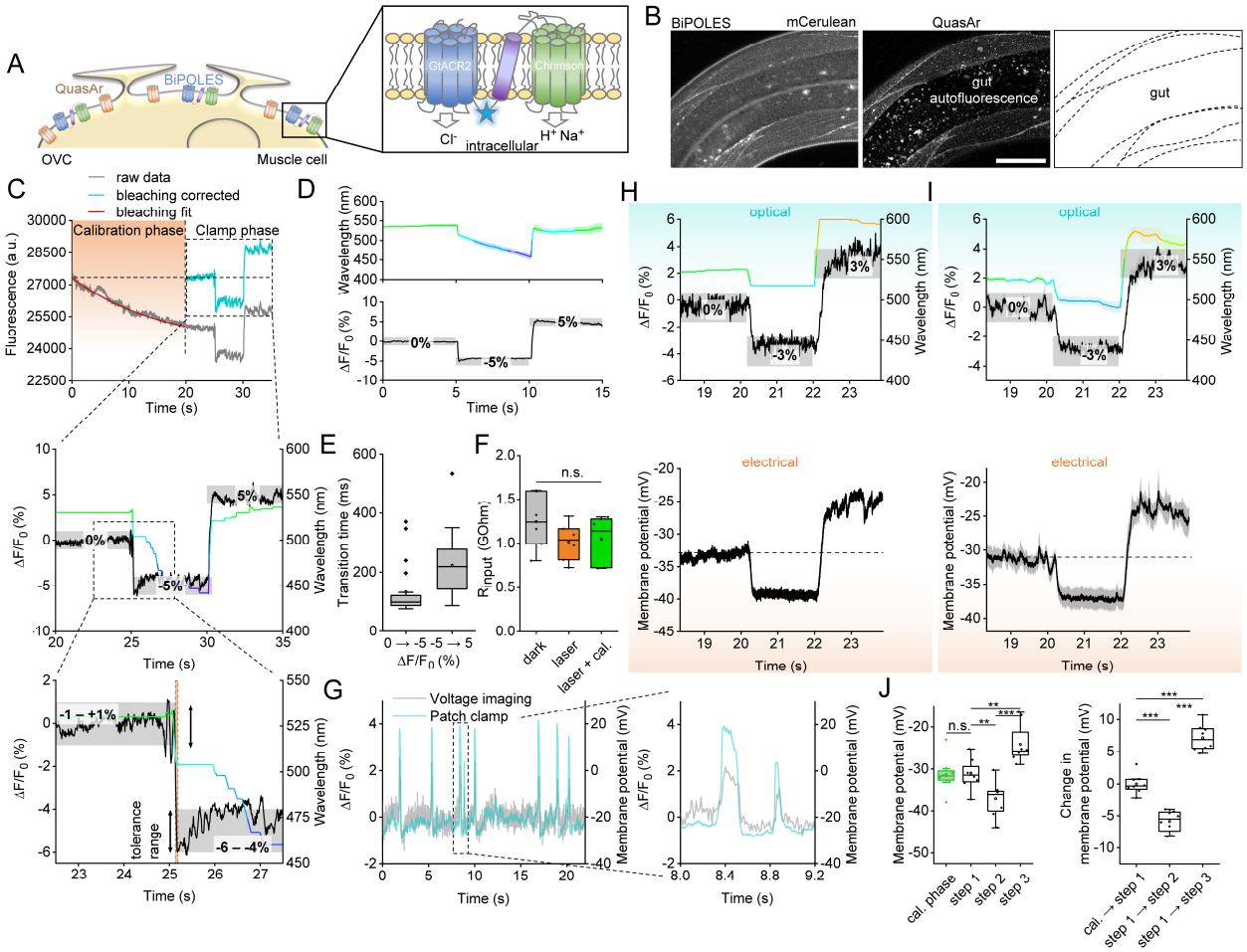

Fig. 2. Bi-directional clamping of membrane voltage in BWMs. (A) OVC (QuasAr2 and BiPOLES; inset, ★: mCerulean) in BWMs. **(B)** Confocal fluorescence z-projection. BiPOLES (mCerulean) and QuasAr2 in BWM membranes, scheme (dashed lines represent muscle plasma membranes). Scale bar, 50 µm. **(C)** OVC three-step protocol (0, -5 and 5 % $\Delta F/F_0$) in BWMs, insets for close-up. Wavelength shown in the respective color, holding values and tolerance range (grey boxes) are indicated for each step. Orange shade in upper panel: transition period to reach tolerance range. **(D)** Upper panel: Overlay of mean (± S.E.M.) wavelength and (lower panel) fluorescence traces (n=22; holding values: 0, -5, 5 % $\Delta F/F_0$). **(E)** Times required for the indicated 5 and 10 % $\Delta F/F_0$ transitions. **(F)** Membrane resistance of BWM cells, before, and during 637 nm laser illumination (orange), and during laser + calibration light; n=6. **(G)** APs in simultaneous patch-clamp and fluorescence recordings during OVC calibration phase (637 nm laser + calibration wavelength). Inset for close-up. **(H)** Example trace of simultaneous patch-clamp and fluorescence recording of an OVC three-step protocol (-3 to +3 % $\Delta F/F_0$). Upper panel: Fluorescence recording with indicated wavelength adaptation and tolerance ranges. Lower panel: Corresponding simultaneous voltage recording. Membrane potential was recorded in whole-cell patch-clamp mode. **(I)** Overlay of mean (± S.E.M.) wavelength, fluorescence (upper panel) and voltage traces (lower panel) of N=4, n=8 measurements as in (H). **(J)** Statistical analysis of data in (I); voltage modulation between transition events during simultaneous OVC measurements (left panel: absolute voltages; right panel: voltage modulation for the respective steps of the OVC protocol). One-way ANOVA with Bonferroni correction. ***P ≤ 0.001, **P ≤ 0.01. In (E, F and J), box plots (median, 25-75th quartiles); mean: open dot; whiskers: 1.5x IQR.

After bleaching correction (R^2 of the exponential fit was always higher than 0.8, in most cases even >0.95; **Extended data Fig. 6B**), the OVC generated incremental changes in wavelength that closely followed the fluctuating fluorescence signals (i.e., membrane voltage; **Fig. 2C**), as soon as the tolerance range for holding $\Delta F/F_0$ was exceeded. Cells were reliably (**Extended data Fig. 6C**), and quickly (**Extended data Fig. 6A**), clamped to holding values between -5 and 5 % $\Delta F/F_0$ (**Fig. 2C, D**), sometimes even -8 to 8 % $\Delta F/F_0$ could be reached (**Extended data Fig. 6F**). This range is smaller than for single-tool experiments (**Extended data Fig. 3D**), since Chrimson and *Gt*ACR2 action spectra partially overlap, and the channels have different conductance [19, 25, 27]. However, due to the bidirectionality and live feedback, the BiPOLES-OVC acted significantly faster, particularly for the return towards resting potential: Transition times were only 147.7 ± 25.5 ms (5→0 %) and 88.0 ± 5.7 ms (-5→0 %) for BiPOLES, compared to 678.6 ± 148.9 ms for ChR2 and 239.5 ± 29.9 ms for *Gt*ACR2 (**Fig. 2E, Extended data Fig. 3G, S6A**). The OVC allowed continuous bidirectional clamping (up to minutes; **Extended data Fig. 5G**), something not achievable with single tools. Once the closed-loop control was interrupted, membrane voltage returned to baseline and higher fluorescence fluctuations were observed (1.87 ± 0.1 vs. 0.78 ± 0.05 % $\Delta F/F_0$ during -5 % clamping; 1.89 ± 0.14 % $\Delta F/F_0$ for animals expressing only QuasAr; **Extended data Fig. 4F**). To extend the applicability of the OVC, we wrote software allowing to select holding $\Delta F/F_0$ values during a running acquisition (**Extended data Fig. 6D-F**), i.e. to respond to observations and to dynamically adapt clamping parameters. The software provides a live status update, whether the OVC system is on hold, adapting or if it has reached its limits (**Extended data Fig. 6D, Extended data video 2**).

Calibrating QuasAr2 fluorescence and membrane potential in BWMs

Next, we determined the actual voltage range that can be adjusted by the OVC. First, we measured membrane voltages and QuasAr2 fluorescence levels in response to wavelength ramps within the margins of the OVC (400-600 nm and *vice versa*). The range of relative fluorescence changes ($\Delta\Delta F/F_0$ at 400-410 and 590-600 nm) was around 16 % (**Extended data Fig. 7A-D**), in line with the range of holding values stably achieved by the OVC (± 8 % $\Delta F/F_0$, **Extended data Fig. 6F**). The corresponding voltage range was around 18 mV (**Extended data Fig. 7D**). The QuasAr2 fluorescence-voltage relation is linear [11], thus we estimated that during -5 to +5 % $\Delta F/F_0$ OVC operation, about 11 mV membrane potential change is achieved. However, these measurements were without OVC feedback. Thus, to directly calibrate the OVC operation range, we concomitantly measured voltage and fluorescence (**Extended data Fig. 7E**). Membrane resistance was not significantly altered by 637 nm laser or compensation light (**Fig. 2F**), and corresponding APs could be observed by fluorescence and patch-clamp before the OVC

clamp phase started (**Fig. 2G**). Concomitant laser (637 nm) and compensation illumination (520 nm) did not alter APs (**Extended data Fig. 7F, G**), and it did not alter membrane potential; however, adding 470 nm light could hyperpolarize the cell by about 16 mV (**Extended data Fig. 7H**). Also, small voltage fluctuations were similar in dark and light conditions by amplitude and frequency (**Extended data Fig. 7I-K**), arguing that membrane resistance of the cells was not altered by the compensation light (**Fig. 2F**). Thus, BiPOLES activation does not lead to general shunting of membrane potential due to open channels. Finally, OVC-induced fluorescence changes (-3 to +3 % $\Delta F/F_0$) modulated voltage by ca. -6 to +7 mV (**Fig. 2H-J**), i.e. ca. 13 mV range per 6 % $\Delta F/F_0$ (22 mV per 10 % $\Delta F/F_0$). This was larger than what we observed by indirect comparison (**Extended data Fig. 7D**), probably due to the live-feedback of the OVC.

Demonstrating homeostatic changes in muscle excitability using the OVC

May the OVC be used to assess divergent cell physiology? *unc-13(n2813)* mutants lack an essential synaptic vesicle priming factor [39] and thus exhibit largely reduced postsynaptic currents upon ChR2-stimulation of motor neurons [40]. Yet, *unc-13* and other neurotransmission mutants showed enhanced muscle contraction when BWMs were directly photostimulated. We hypothesized that muscles homeostatically change their excitability. To explore if the OVC can detect this, we induced a +5 % $\Delta F/F_0$ depolarization step: Indeed, in *unc-13(n2813)* mutants the OVC required significantly blue shifted light (i.e., less Chrimson activation) to induce the same level of depolarization as in wild type (534.2 ± 2.8 vs. 550.4 ± 3.1 nm; **Fig. 3A, B**). Muscles in *unc-13* animals may exhibit higher excitability to balance the lower excitatory input they receive. Though membrane resistance was unaltered (**Fig. 3C**), the amplitude of induced voltage increases was higher in *unc-13* mutants when we injected current ramps (**Fig. 3D-F**). Similarly, APs measured by voltage imaging were significantly increased by amplitude and duration (**Fig. 3G-J**). This indicates that in response to a lack of presynaptic input, ion channels shaping muscle voltage / APs, i.e. voltage-gated Ca^{2+} (EGL-19) and K^+ channels (SLO-2, SHK-1) [41, 42], may undergo homeostatic changes to enable the observed higher muscle excitability.

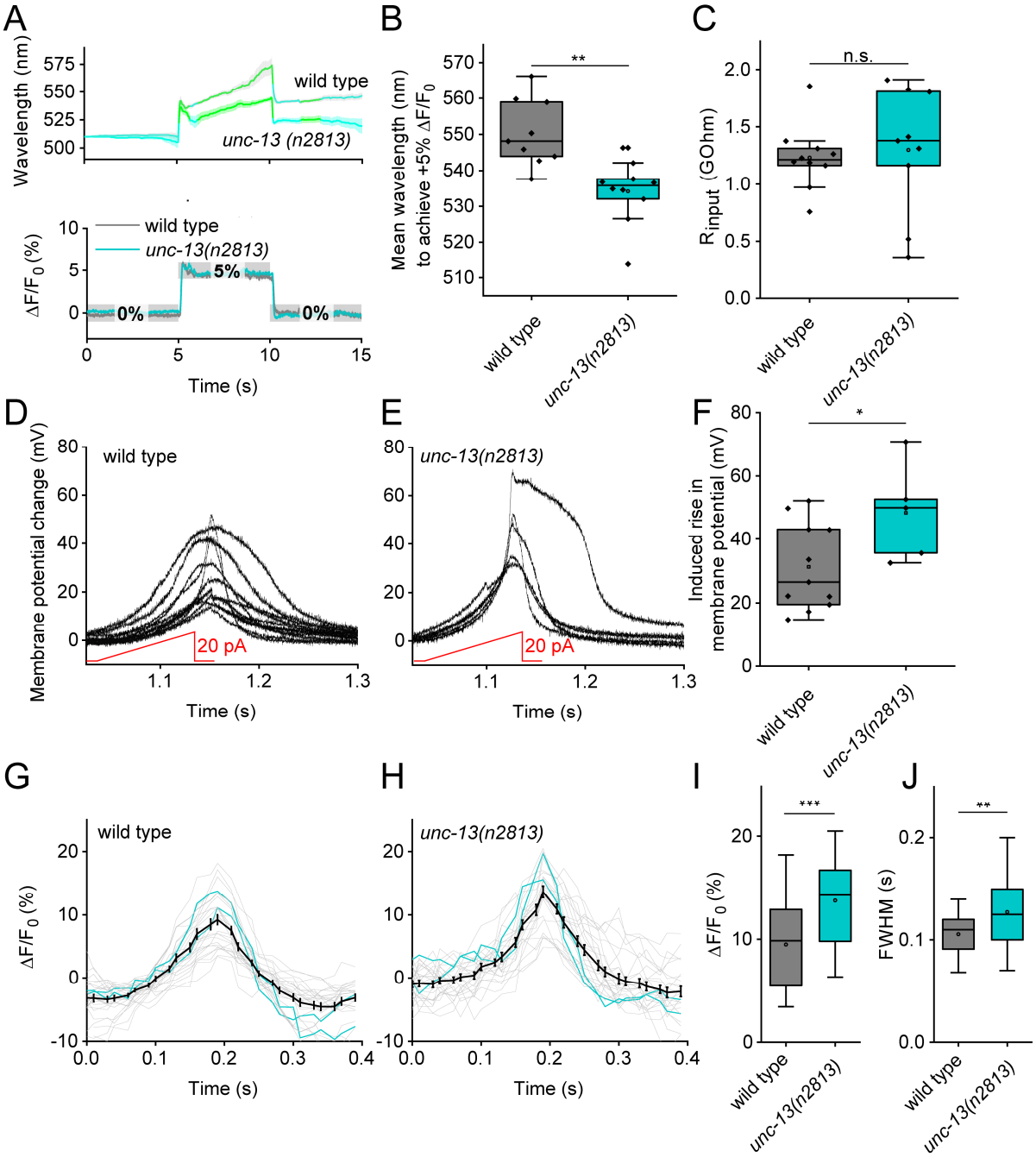

Fig. 3. Assessing altered cell physiology in mutants, using the OVC. (A) *unc-13(n2813)* mutant and wild type animals were subjected to OVC depolarization, to +5 % $\Delta F/F_0$. Mean wavelength traces (± S.E.M.), n = 9-10. **(B)** Mean wavelength required during the depolarization step, required to hold +5 % $\Delta F/F_0$. **(C)** Membrane resistance was analyzed in wild type and *unc-13* mutant muscles. n = 9-10. **(D, E)** Current ramps (0-20 pA over 100 ms; red) were injected into wild type and *unc-13* mutant muscles and the induced voltage increases were aligned to the peak. n = 5-11. **(F)** Group data of induced voltage increases in (D and E). **(G, H)** Optical recordings of spontaneous APs in *unc-13* mutants and wild type animals. Overlay of single (each two are highlighted in cyan) and mean (± S.E.M.) traces. n = 26-27. **(I, J)** Statistical analysis of peak AP amplitude and AP duration (at FWHM) of data in (G and H). Two-sided t-test with Bonferroni correction in (B, C, F, I, J). ***P ≤ 0.001, **P ≤ 0.01, *P ≤ 0.05 and box plots (median, 25-75th quartiles); mean: open dot; whiskers: 1.5x IQR.

OVC in cholinergic and GABAergic motor neurons

We tested if the OVC works also in *C. elegans* neurons. Cholinergic and GABAergic motor neurons are small (ca. 2-3 µm cell body, BWMs ca. 50 µm) and exhibit low absolute fluorescence. Both mCerulean (BiPOLES) and QuasAr2 fluorescence were observed in respective ganglia, including the anterior nerve ring and ventral nerve cord (**Fig. 4A, B**). Calibration parameters could be adopted from muscle experiments (**Fig. 4C**). The OVC could readily clamp neuronal voltage-dependent fluorescence between -5 and 5 % $\Delta F/F_0$ (**Fig. 4C-G**), and also adaptive experiments were possible (**Extended data Fig. 6G, H**).

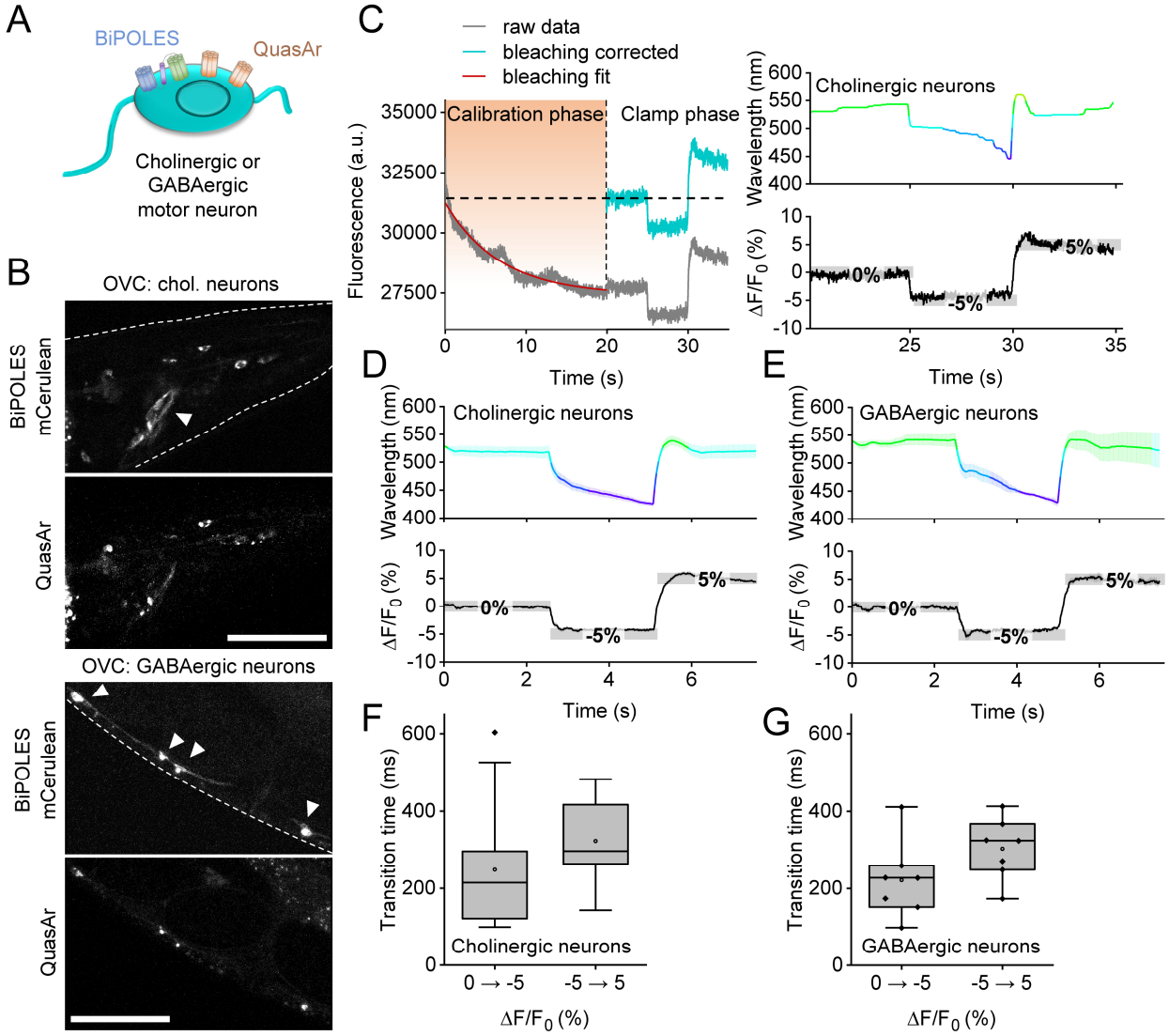

Fig. 4. Bi-directional clamping of voltage-dependent fluorescence in *C. elegans* neurons. (A) OVC in cholinergic or GABAergic neurons. **(B)** Confocal fluorescence z-projections of BiPOLES (mCerulean) and QuasAr2 expression. Arrowheads: Neuronal cell bodies. Scale bars: 50 µm. **(C)** OVC protocol (holding values 0, -5, 5 % $\Delta F/F_0$) in cholinergic neurons, single recording. **(D, E)** Mean (± S.E.M.) traces of the OVC in cholinergic (D; n = 14), or GABAergic (E, n = 7) neurons, respectively, holding values: 0, -5, 5 % $\Delta F/F_0$. **(F, G)** Transition times for 5 and 10 % $\Delta F/F_0$ steps (F: cholinergic, G: GABAergic neurons); box plots (median, 25-75th quartiles), mean: open dot, whiskers: 1.5x IQR.

In mammalian neurons, the OVC acts as an optogenetic conductance-clamp

Rodent neurons are larger, more hyperpolarized cells and display faster AP kinetics than *C. elegans* muscles and neurons. Since such cells are relevant to studies of human-like neurophysiology, we explored the utility of the OVC in rat hippocampal pyramidal neurons (organotypic slice culture; **Fig. 5A**), expressing QuasAr2 and soma-targeted (som)BiPOLES.

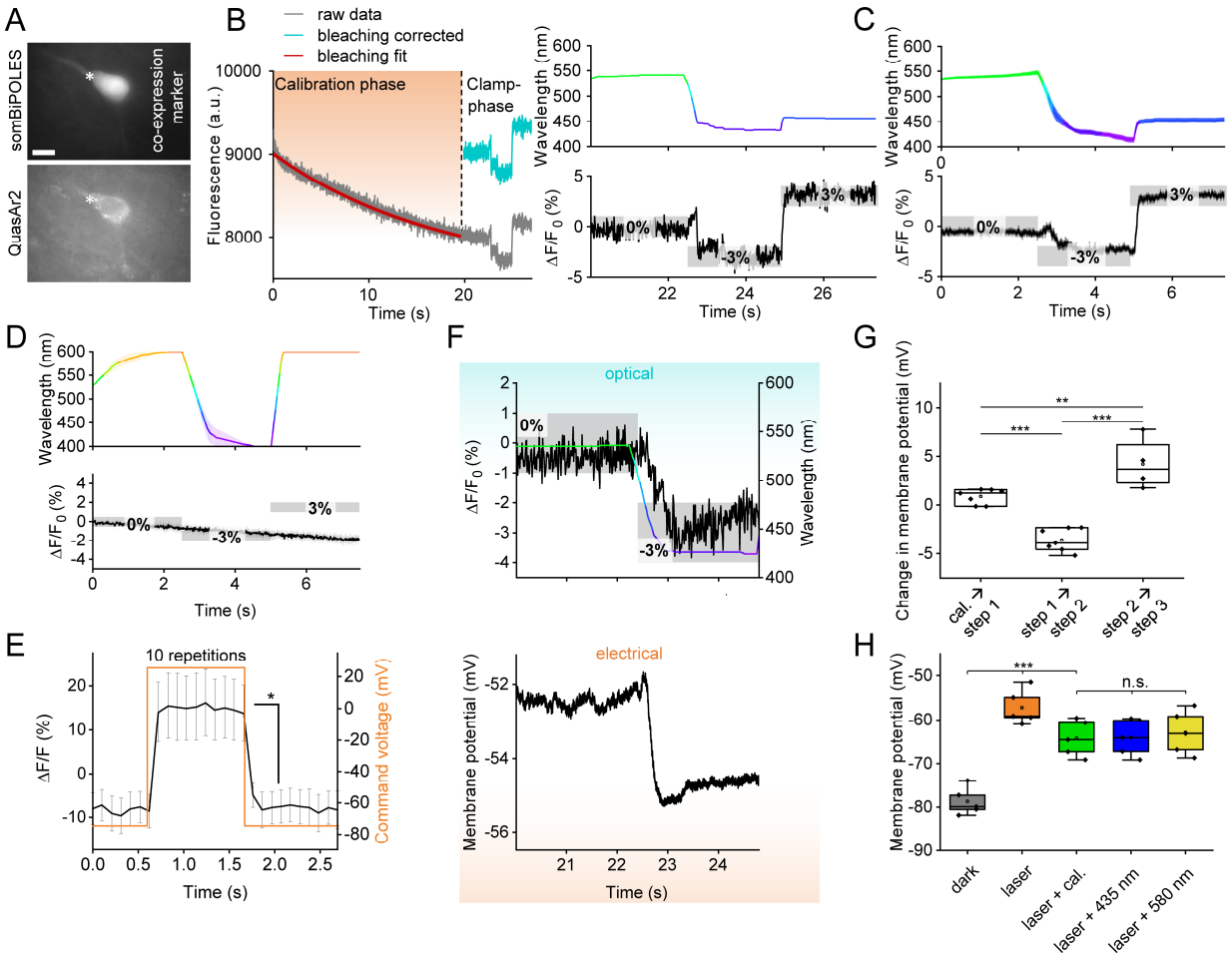

Fig. 5. Establishing the OVC in rat hippocampal pyramidal neurons. (A) Fluorescence micrographs of somBiPOLES (CFP co-expression marker) and QuasAr2 expression in a neuron (asterisk). Scale bar: 10 µm. **(B)** OVC three-step protocol (0, -3 and 3 % $\Delta F/F_0$). Right: Wavelength shown in the respective color (upper), holding values and tolerance range (grey boxes, lower panel) are indicated for each step. Left: Orange shade marks transition/calibration period to reach tolerance range. **(C)** Overlay of mean (± S.E.M.) wavelength (upper panel) and fluorescence traces (lower panel; n=12; holding values: 0, -3, 3 % $\Delta F/F_0$). **(D)** Average fluorescence data (lower panel) for cells expressing QuasAr2 only, while the OVC attempts to run a 0, -3, 3 % $\Delta F/F_0$ protocol (n = 5; upper panel: Monochromator wavelength). **(E)** QuasAr2 fluorescence during electrically evoked 100 mV depolarization step, from -74.5 mV to +25.5 mV holding voltage. **(F)** Simultaneous patch-clamp (voltage, lower panel) and fluorescence recording (upper panel) with indicated wavelength adaptation and tolerance ranges. **(G)** Statistical analysis of voltage modulation between transition events during simultaneous patch clamp / OVC measurements (n = 3-7). **(H)** Modulation of membrane voltage in cells expressing somBiPOLES only, in response to different light application, as indicated. One-way ANOVA with Bonferroni correction. ***P ≤ 0.001, **P ≤ 0.01, *P ≤ 0.05; n = 3-7. In (G, H), box plots (median, 25-75th quartiles); mean: open dot; whiskers: 1.5x IQR.

After bleaching calibration (**Fig. 5B**), optical clamping could be achieved between ± 3 % $\Delta F/F_0$ (**Fig. 5B, C**) with the OVC protocol as used in *C. elegans*. Importantly, in the absence of somBiPOLES, monochromator light did not lead to modulation of QuasAr2 fluorescence (**Fig. 5D**), while electrically evoked potential shifts (100 mV depolarization step, from -74.5 mV to +25.5 mV holding voltage) caused clear increases of QuasAr2 fluorescence (ca. 21 % $\Delta F/F_0$; **Fig. 5E**). In cells expressing QuasAr2 and somBiPOLES, the ± 3 % $\Delta F/F_0$ OVC protocol caused hyperpolarizing and depolarizing potential jumps (ca. - 4 mV and + 3 mV, respectively; **Fig. 5F, G**). These were small, compared to earlier experiments using somBiPOLES, where 595 nm light application caused depolarization of up to 30 mV, while 400 nm light clamped cells to the Cl^- reversal potential [26]. Possibly, due to the more negative resting potential in mammalian neurons compared to *C. elegans* cells, 637 nm activation of Chrimson causes stronger effects, and thus the OVC triggers more compensatory GtACR2 currents. When we expressed somBiPOLES only, 637 nm laser light depolarized hippocampal neurons (via Chrimson) by ca. 21.5 mV, which could be partially counteracted by GtACR2 activation using 530 nm compensation light (**Fig. 5H**). However, due to the high conductance of GtACR2, shunting effects likely prevented further optical hyper- or depolarization. Thus, in mammalian neurons, the OVC works with a limited range, likely due to different voltage and ion conditions in the resting state, and acts more as a 'conductance-clamp'.

Dynamic suppression of muscle APs

Thus far, we imposed fixed voltage steps to cells. To see if the OVC can dynamically counteract spontaneous activity, as opposed to shunting hyperpolarization, we turned to a periodically active muscular pump, the *C. elegans* pharynx (**Fig. 6A**). This feeding organ exhibits periodic, ca. 4 Hz APs [20], triggered by serotonin. Closing of the grinder, a structure used to crush bacteria, was triggered by activation of *Gt*ACR2 (400 nm), and could be observed by QuasAr2 fluorescence (**Extended data Fig. 8A**), while illumination with only the 637 nm laser caused grinder opening. The OVC could clamp the pharynx between -5 and 5 % $\Delta F/F_0$ (**Fig. 6B, C, Extended data Fig. 8B-D**). Optically observed APs show a rise time constant of around 15 ms and duration of ca. 150 ms (at full-width-half-maximum - FWHM) [20]. To clamp these APs dynamically, i.e., to counteract de- and repolarization phases quickly enough, we altered the OVC software to respond with more pronounced wavelength changes to a given fluorescence change (increased integral gain; methods, **equation 6**), and reduced the tolerance range to ± 0.005 %. During calibration, APs showed 30.1 ± 1.1 % $\Delta F/F_0$ mean amplitude and 120 ± 4 ms duration at FWHM (**Fig. 6B, C, E, F**). Upon clamping, all subsequent attempts to spike were dynamically counteracted and almost completely suppressed (**Fig. 6B-F**). AP amplitude was significantly reduced to ca. 2 % (**Fig. 6E,**

F), as was AP duration (to 82.6 ± 3.3 ms at FWHM). Clamping was rapid: APs occurring at clamping onset were shortened by 65 %, while the OVC traversed the full wavelength spectrum within 20 ms (**Fig. 6D**).

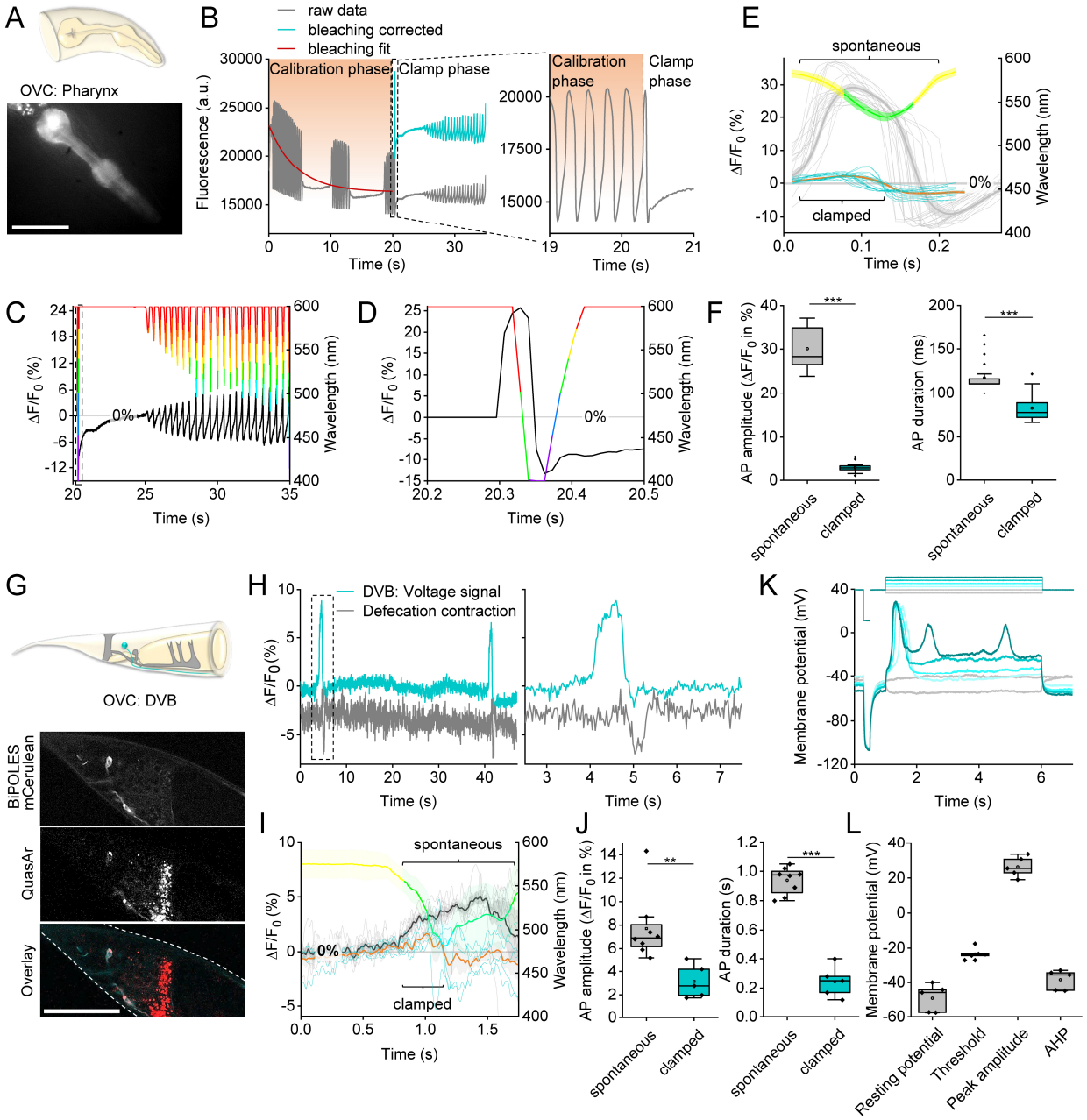

Fig. 6. All-optical clamping of APs in pharyngeal muscle and the enteric motor neuron DVB. (A) The *C. elegans* pharynx, a muscular pump used for feeding, expressing the OVC (QuasAr2 fluorescence). **(B-D)** OVC experiment in pharyngeal muscle, to hold fluorescence at 0% $\Delta F/F_0$ and suppress APs. (B) Original trace, calibration, and clamping phase. Inset shows close-up of boxed region, transition from calibration to clamp phase. (C) Overlay of wavelength and $\Delta F/F_0$ traces during clamp phase. (D) Close-up of region boxed in (C): OVC counteracting first AP during clamp phase. **(E)** Aligned traces of spontaneous (light grey, n=20) and clamped (blue, n=20) pharyngeal fluorescence signals. Mean wavelength chosen by the system is shown in the respective color. **(F)** Statistical analysis of data in (E), fluorescence voltage signal amplitude and duration at FWHM. **(G)** The GABAergic motor neuron DVB (cyan) innervates enteric

muscles (grey, upper panel). Below: Confocal z-projection of BiPOLES and QuasAr2 fluorescence in DVB, and overlay; scale bar: 50 µm. **(H)** Voltage fluorescence signals of spontaneous APs in DVB (blue trace). Expulsion muscle contraction, deduced from DVB cell body movement, shown as gray trace. Right panel: Close-up of boxed region. **(I)** Overlay of spontaneous (light gray traces, n=8; mean: black) and clamped (blue traces, n=5; mean: orange) DVB voltage signals. Mean wavelength set by the OVC shown in the respective color. **(J)** Statistical analysis of data in (I), mean voltage fluorescence signal amplitude and total duration. **(K)** Current clamp recordings (n=5, lower panel) of DVB in dissected animals, following indicated (upper panel) hyperpolarizing (grey) and depolarizing (cyan) injection of current in 1 pA steps. **(L)** Group data of (K): resting potential, threshold, peak amplitude, duration at FWHM, and afterhyperpolarization (AHP). In (F, J and L): box plots (median, 25-75th quartiles), mean: open dot, whiskers: 1.5x IQR. In (F and L), two-sided t-test with Bonferroni correction. ***P ≤ 0.001, **P ≤ 0.01.

Clamping APs in the GABAergic motor neuron DVB

C. elegans exhibits a rhythmic motor program to move and expel gut contents [28-31]. Expulsion muscle contraction is regulated by an intestinal pacemaker and by GABAergic motor neurons DVB and AVL (**Fig. 6G**). Ca^{2+} imaging of DVB [43] revealed activity reminiscent of APs, thus far observed in only few *C. elegans* neurons [44]. DVB voltage imaging showed APs (7.7 ± 1 % $\Delta F/F_0$, 500 ± 60 ms at FWHM) at regular time intervals of 40-50 s, that were followed by posterior body contraction (**Fig. 6H**). Using parameters as for the pharynx, DVB APs were clamped to significantly reduced amplitude and duration (**Fig. 6I, J**; see **Extended data Fig. 8E** for single trace). DVB allowed calibrating the neuronal OVC by patch-clamp electrophysiology [45]: Resting potential was -49.0 ± 8.9 mV (**Fig. 6K, L**), and increasing current steps (1 pA) evoked APs (-23.4 mV threshold, depolarization to 26.3 mV, 359 ms duration (FWHM), -38.5 mV afterhyperpolarization; n=5 cells; **Fig. 6L**). DVB AP amplitude thus is ca. 50 mV. Although fluorescence baseline may be altered by the 637 nm laser and Chrimson activation, this did not evoke APs. Thus, the QuasAr2 signal in DVB, i.e., 7.7 % $\Delta F/F_0$ for an AP, corresponds to ca. 50 mV (calculating from threshold, or up to 75 mV, from resting potential).

Discussion

Here, we established the OVC, the first all-optical voltage-clamp approach to date. We demonstrated its performance in various excitable cell types in intact animals (*C. elegans*) and tested it in mammalian hippocampal neurons. In *C. elegans*, the OVC allowed reliable clamping of voltage in two muscular organs and three neuron types *via* QuasAr2 fluorescence read-out and bidirectional optogenetic actuation *via* BiPOLES. The OVC could further detect the altered postsynaptic excitability of *unc-13* mutants, a homeostatic response to reduced presynaptic input. Using the OVC, we did not only control resting membrane potential, but could also dynamically clamp spontaneous rhythmic activity and APs in pharyngeal muscle and in the motor neuron DVB. The OVC operates at rates up to 90 Hz on a typical PC with moderate computing power, which

372 orchestrates the communication between camera and monochromator, while in parallel running
373 image acquisition and providing live computation of bleaching-corrected $\Delta F/F_0$ values, fed into a
374 decision tree and Integral-control algorithm. An alternative algorithm with PID controller and
375 Kalman filter provided more accurate clamping, though it did not increase system speed. While
376 the OVC at present is slower and less sensitive than standard patch-clamp electrophysiology, it
377 outperforms it in terms of non-invasiveness, throughput and ease of application. In mammalian
378 neurons, likely due to different physiology, the OVC in its current composition of light-gated ion
379 channels and QuasAr2 worked as a conductance clamp. However, in *C. elegans*, though
380 activation of Chrimson by the QuasAr2 excitation light affects baseline physiology, this effect
381 could be counterbalanced by utilizing the bidirectional control properties of BiPOLES, using a
382 compensation wavelength. No adverse effects on membrane resistance were observed (**Fig. 2F**),
383 it did not affect membrane potential, intrinsic neuronal activity and cellular excitability, as judged
384 by voltage fluctuations in muscle (**Extended data Fig. 7H-K**), muscles fired normal APs
385 (**Extended data Figs. 4F, 7F, G**), locomotion behavior was unaltered (**Extended data Fig. 5E,**
386 **F**), and also spontaneous activity in pharyngeal muscle or the DVB neuron was unaffected.
387 The voltage range covered by the OVC differed between muscles and neurons: 10 % $\Delta F/F_0$
388 change corresponded to about 22 mV in BWMs, and to about 65 mV in DVB. Differences in
389 membrane potential and AP amplitude depend on the different ion channels and gradients present
390 in the two cell types. The different range of $\Delta F/F_0$ fluorescence of QuasAr2 in muscles and
391 neurons may correspond to a different surface to volume ratio of the two cell types, and possibly,
392 different levels of QuasAr2 protein in plasma membrane vs. intracellular membranes.
393 Fluorescence from the latter would not contribute to voltage-dependent $\Delta F/F_0$, while it would
394 increase overall fluorescence at rest.
395 In mammalian neurons, optical voltage control was currently limited to a few mV. This may in
396 part be due to the high expression levels of BiPOLES, and in part due to the low electrochemical
397 gradient for Cl^-, as the resting potential is close to the Nernst potential for Cl^-. Thus, in comparison
398 to *C. elegans*, more activation of GtACR2 is required to counteract Chrimson-based
399 depolarization, causing membrane leak. Minimizing the optical crosstalk of voltage sensor and
400 BiPOLES is especially important in mammalian neurons. Further red-shifted voltage sensors and
401 blue-shifted BiPOLES variants are thus required for future OVC experiments. The membrane leak
402 in mammalian neurons makes the OVC a 'conductance-clamp'. Light-driven ion pumps, provided
403 they become as powerful as the channels used here, could be a future alternative.
404 The speed of the OVC is currently limited by the sensitivity, fluorescence yield, dynamic range
405 of the GEVI (requiring 10 ms exposure times) and its time constant, the camera frame rate, and
406 the computer hardware. With higher fluorescence change in response to membrane potential and

407 a larger absolute GEVI fluorescence (i.e., improved signal to noise ratio), higher frame rates could
408 potentially be achieved. The software component currently runs within µManager on a PC.
409 Running the software on an integrated circuit, like a field programmable gate array (FPGA), and
410 using a faster camera may enable faster operation speeds up to 1 kHz. GEVI kinetics is not likely
411 to become a limiting factor, as QuasAr2 has been shown to faithfully report on single APs in
412 mammalian neurons (2 ms), clearly showing AP rise and repolarization phases [11]. OFF kinetics
413 of the actuators may pose a limit to the maximal response times of the OVC: These are ca. 21-
414 45 ms for Chrimson, for which, however, a 10 times faster variant has been isolated [24, 25], and ca.
415 40 ms for *Gt*ACR2; also here, a 20 times faster ZipACR was described [46]. However, due to
416 BiPOLES, fast OFF kinetics are less important, as it enables active counteraction. Since channel
417 ON kinetics are generally faster, they are also not likely to limit the maximal speed achievable by
418 the OVC.

419 The OVC detected altered muscular excitability in *C. elegans unc-13* mutants, which is likely
420 caused by changes in ion channel physiology. This shows that the OVC represents an approach
421 to enable all-optical, contact-less high-throughput screening applications, e.g. of compound
422 libraries targeted at ion channels. Testing its use in mammalian cell types other than neurons,
423 where such ion channels can be expressed individually, and where the resting membrane
424 potential is less depending on the Cl^- gradient, will facilitate this approach.

425 The establishment of the OVC paves the way for all-optical control of individual neurons in
426 freely behaving transparent animals like *C. elegans*. Accuracy of fluorescence quantification (and
427 thus OVC feedback) requires the cell to remain in focus, which can be achieved with the OVC,
428 while it is impossible to keep a patch-clamp electrode physically attached to such small animala.
429 Using the OVC on neurons controlling behavior will allow fine-tuning of, and enable understanding
430 how activity of the individual cell regulates, behavioral aspects. Online behavioral analysis (e.g.
431 extent of body bending, locomotion velocity), may be used to feedback to the neuron such that
432 behavior can be dynamically controlled.

433 Transferring the OVC to other model organisms may require modifications depending on the
434 respective cellular properties. Extending electrophysiology applications, the OVC will enable
435 efficient space clamp, as well as dynamic local clamping in neuronal processes. The OVC
436 software is universally applicable, as it can be easily adapted to other GEVI-optogenetic actuator
437 combinations. The OVC broadens applicability of optogenetics as it allows modulation in closed-
438 loop, as opposed to static optical perturbation that cannot adapt to the variable activity patterns
439 found in living organisms. Dynamic responsiveness is also advantageous with regard to future
440 therapeutic applications, for example in acute control of seizures [47], or in adaptive deep brain
441 stimulation, as it would allow adjusting the therapy to the need of the patient [48].

References

1. Bargmann, C.I. & Marder, E. From the connectome to brain function. *Nat Methods* **10**, 483-490 (2013).
2. Anderson, D.J. Circuit modules linking internal states and social behaviour in flies and mice. *Nat Rev Neurosci* **17**, 692-704 (2016).
3. Rajasethupathy, P., Ferenczi, E. & Deisseroth, K. Targeting Neural Circuits. *Cell* **165**, 524-534 (2016).
4. Francis, M.M., Mellem, J.E. & Maricq, A.V. Bridging the gap between genes and behavior: recent advances in the electrophysiological analysis of neural function in Caenorhabditis elegans. *Trends Neurosci* **26**, 90-99 (2003).
5. Liu, P., Chen, B. & Wang, Z.-W. GABAergic motor neurons bias locomotor decision-making in C. elegans. *Nature communications* **11**, 5076 (2020).
6. Noguchi, A., Ikegaya, Y. & Matsumoto, N. In Vivo Whole-Cell Patch-Clamp Methods: Recent Technical Progress and Future Perspectives. *Sensors (Basel)* **21** (2021).
7. Akerboom, J. et al. Genetically encoded calcium indicators for multi-color neural activity imaging and combination with optogenetics. *Frontiers in molecular neuroscience* **6**, 2 (2013).
8. Chen, T.W. et al. Ultrasensitive fluorescent proteins for imaging neuronal activity. *Nature* **499**, 295-300 (2013).
9. Lin, M.Z. & Schnitzer, M.J. Genetically encoded indicators of neuronal activity. *Nat Neurosci* **19**, 1142-1153 (2016).
10. Kralj, J.M., Douglass, A.D., Hochbaum, D.R., Maclaurin, D. & Cohen, A.E. Optical recording of action potentials in mammalian neurons using a microbial rhodopsin. *Nat Methods* **9**, 90-95 (2012).
11. Hochbaum, D.R. et al. All-optical electrophysiology in mammalian neurons using engineered microbial rhodopsins. *Nat Methods* **11**, 825-833 (2014).
12. Fan, L.Z. et al. All-Optical Electrophysiology Reveals the Role of Lateral Inhibition in Sensory Processing in Cortical Layer 1. *Cell* **180**, 521-535 e518 (2020).
13. Piatkevich, K.D. et al. A robotic multidimensional directed evolution approach applied to fluorescent voltage reporters. *Nat Chem Biol* **14**, 352-360 (2018).
14. Knopfel, T. & Song, C. Optical voltage imaging in neurons: moving from technology development to practical tool. *Nat Rev Neurosci* **20**, 719-727 (2019).
15. Gong, Y., Wagner, M.J., Zhong Li, J. & Schnitzer, M.J. Imaging neural spiking in brain tissue using FRET-opsin protein voltage sensors. *Nature communications* **5**, 3674 (2014).
16. Gong, Y., Li, J.Z. & Schnitzer, M.J. Enhanced Archaerhodopsin Fluorescent Protein Voltage Indicators. *PLoS One* **8**, e66959 (2013).
17. Maclaurin, D., Venkatachalam, V., Lee, H. & Cohen, A.E. Mechanism of voltage-sensitive fluorescence in a microbial rhodopsin. *Proc Natl Acad Sci U S A* **110**, 5939-5944 (2013).
18. Flytzanis, N.C. et al. Archaerhodopsin variants with enhanced voltage-sensitive fluorescence in mammalian and Caenorhabditis elegans neurons. *Nature communications* **5**, 4894 (2014).
19. Bergs, A. et al. Rhodopsin optogenetic toolbox v2.0 for light-sensitive excitation and inhibition in Caenorhabditis elegans. *PLoS One* **13**, e0191802 (2018).
20. Azimi Hashemi, N. et al. Rhodopsin-based voltage imaging tools for use in muscles and neurons of Caenorhabditis elegans. *Proc Natl Acad Sci U S A* **116**, 17051-17060 (2019).
21. Kannan, M. et al. Fast, in vivo voltage imaging using a red fluorescent indicator. *Nat Methods* **15**, 1108-1116 (2018).
22. Streit, J. & Kleinlogel, S. Dynamic all-optical drug screening on cardiac voltage-gated ion channels. *Scientific reports* **8**, 1153 (2018).
23. Newman, J.P. et al. Optogenetic feedback control of neural activity. *eLife* **4**, e07192 (2015).
24. Klapoetke, N.C. et al. Independent optical excitation of distinct neural populations. *Nat Methods* **11**, 338-346 (2014).
25. Oda, K. et al. Crystal structure of the red light-activated channelrhodopsin Chrimson. *Nature communications* **9**, 3949 (2018).
26. Vierock, J. et al. BiPOLES is an optogenetic tool developed for bidirectional dual-color control of neurons. *Nature communications* **12**, 4527 (2021).
27. Govorunova, E.G., Sineshchekov, O.A., Janz, R., Liu, X. & Spudich, J.L. NEUROSCIENCE. Natural light-gated anion channels: A family of microbial rhodopsins for advanced optogenetics. *Science* **349**, 647-650 (2015).
28. Shtonda, B. & Avery, L. CCA-1, EGL-19 and EXP-2 currents shape action potentials in the Caenorhabditis elegans pharynx. *J Exp Biol* **208**, 2177-2190 (2005).
29. Beg, A.A. & Jorgensen, E.M. EXP-1 is an excitatory GABA-gated cation channel. *Nat Neurosci* **6**, 1145-1152 (2003).
30. McIntire, S.L., Jorgensen, E., Kaplan, J. & Horvitz, H.R. The GABAergic nervous system of Caenorhabditis elegans. *Nature* **364**, 337-341 (1993).
31. Avery, L. & Thomas, J.H. in C. elegans II. (eds. nd, D.L. Riddle, T. Blumenthal, B.J. Meyer & J.R. Priess) (Cold Spring Harbor (NY); 1997).
32. Zhang, F. et al. Multimodal fast optical interrogation of neural circuitry. *Nature* **446**, 633-639 (2007).
33. Nagel, G. et al. Light activation of channelrhodopsin-2 in excitable cells of Caenorhabditis elegans triggers rapid behavioral responses. *Curr Biol* **15**, 2279-2284 (2005).

34. Edelstein, A., Amodaj, N., Hoover, K., Vale, R. & Stuurman, N. Computer Control of Microscopes Using µManager. (John Wiley & Sons, Inc., 2010).
35. Foellinger, O., Doerrscheidt, F. & Klittich, M. Regelungstechnik, Edn. 12th. (Vde Verlag, 2016).
36. Kalman, R.E. A New Approach to Linear Filtering and Prediction Problems. *J. Basic Eng.* **82**, 35-45 (1960).
37. Nagel, G. et al. Channelrhodopsins: directly light-gated cation channels. *Biochem Soc Trans* **33**, 863-866 (2005).
38. Zou, P. et al. Bright and fast multicoloured voltage reporters via electrochromic FRET. *Nature communications* **5**, 4625 (2014).
39. Richmond, J.E., Davis, W.S. & Jorgensen, E.M. UNC-13 is required for synaptic vesicle fusion in C. elegans. *Nat Neurosci* **2**, 959-964 (1999).
40. Liewald, J.F. et al. Optogenetic analysis of synaptic function. *Nat Methods* **5**, 895-902 (2008).
41. Liu, P. et al. Genetic dissection of ion currents underlying all-or-none action potentials in C. elegans body-wall muscle cells. *J Physiol* **589**, 101-117 (2011).
42. Gao, S. & Zhen, M. Action potentials drive body wall muscle contractions in Caenorhabditis elegans. *Proc Natl Acad Sci U S A* **108**, 2557-2562 (2011).
43. Wang, H. & Sieburth, D. PKA controls calcium influx into motor neurons during a rhythmic behavior. *PLoS Genet* **9**, e1003831 (2013).
44. Liu, Q., Kidd, P.B., Dobosiewicz, M. & Bargmann, C.I. C. elegans AWA Olfactory Neurons Fire Calcium-Mediated All-or-None Action Potentials. *Cell* **175**, 57-70 e17 (2018).
45. Jiang, J. et al. C. elegans enteric motor neurons fire synchronized action potentials underlying the defecation motor program. *bioRxiv*, 2021.2008.2025.457687 (2021).
46. Govorunova, E.G. et al. The Expanding Family of Natural Anion Channelrhodopsins Reveals Large Variations in Kinetics, Conductance, and Spectral Sensitivity. *Scientific reports* **7**, 43358 (2017).
47. Paz, J.T. et al. Closed-loop optogenetic control of thalamus as a tool for interrupting seizures after cortical injury. *Nat Neurosci* **16**, 64-70 (2013).
48. Widge, A.S., Malone, D.A., Jr. & Dougherty, D.D. Closing the Loop on Deep Brain Stimulation for Treatment-Resistant Depression. *Frontiers in neuroscience* **12**, 175 (2018).
49. Adam, Y. et al. Voltage imaging and optogenetics reveal behaviour-dependent changes in hippocampal dynamics. *Nature* **569**, 413-417 (2019).
50. Gradinaru, V. et al. Molecular and cellular approaches for diversifying and extending optogenetics. *Cell* **141**, 154-165 (2010).
51. Mahn, M. et al. High-efficiency optogenetic silencing with soma-targeted anion-conducting channelrhodopsins. *Nature communications* **9**, 4125 (2018).
52. Schindelin, J., Rueden, C., Miura, K., Hiner, M. & Tinevez, J.-Y. CorrectBleach: upgrade with Exponential fitting method. (2016).
53. Schindelin, J. et al. Fiji: an open-source platform for biological-image analysis. *Nature Methods* **9**, 676-682 (2012).
54. Kim, P. Kalman Filter for Beginners: with MATLAB Examples, Edn. 1st. (CreateSpace Independent Publishing Platform, 2011).
55. Gee, C.E., Ohmert, I., Wiegert, J.S. & Oertner, T.G. Preparation of Slice Cultures from Rodent Hippocampus. *Cold Spring Harbor protocols* **2017** (2017).
56. Wiegert, J.S., Gee, C.E. & Oertner, T.G. Viral Vector-Based Transduction of Slice Cultures. *Cold Spring Harbor protocols* **2017** (2017).
57. Wiegert, J.S., Gee, C.E. & Oertner, T.G. Single-Cell Electroporation of Neurons. *Cold Spring Harbor protocols* **2017** (2017).

Acknowledgements

We thank Jiajie Shao for support in confocal microscopy, Adam Cohen for reagents, and Sven Plath, Regina Wagner, Hans-Werner Müller, Franziska Baumbach, Nico Sturman, Adrian Breicher, Timotheus Kozlowski, and Kathrin Sauter for expert technical assistance.

Funding

Goethe University (AG); Deutsche Forschungsgemeinschaft, SFB807/B02 (AG), SPP1926-XIb / WI 4485/3-2 (JSW), and SFB1315/C01 (JV, PH); Max Planck Society, PhD fellowship (ACFB); Chan Zuckerberg Initiative, support (QL, CIB)

Author contributions

Conceptualization: ACFB, AG, JSW

Methodology: ACFB, AB, JV, PH, JSW

Investigation: ACFB, JFL, SRR, QL, AN, CW, NZ, HD

Visualization: ACFB, AG

Funding Acquisition: AG, ACFB, JSW, PH, CIB

Project administration: AG

Supervision: AG, JSW, CIB

Writing – original draft: ACFB, AG

Writing – review & editing: ACFB, AG, SRR, JSW, JV, CIB, PH

Competing Interests

A patent application has been filed: EP 21162331.9 (ACFB, AG).

Data and materials availability

The datasets generated during and/or analyzed during the current study are available from the corresponding author on reasonable request. This also applies to materials described in the study.

Software availability

The software / code used for operating the OVC is written in beanshell, the scripting language used by µManager freeware. Two scripts ("OVC_main_script", "OVC_on_the_run_mode") are available as a supplementary files. They will be made available upon publication under the license XYZ.

Extended data

Online Methods

Extended data Figures 1 to 8

Extended data videos 1 and 2

582 # Online Methods

583 **Transgenic *C. elegans* strains**

584 The following strains were used or generated, and are available upon request: **ZX2476**:
585 *zxEx1139[pmyo-3::QuasAr2; pmyo-2::CFP]*, **ZX2482**: *zxEx1145[pmyo-3::QuasAr2; pmyo-*
586 *2::CFP]; zxIs5[punc-17::ChR2(H134R)::yfp;lin-15+]*, **ZX2483**: *zxEx1146[punc-17::ACR2::eYFP;*
587 *pmyo-3::QuasAr2; pelt-2::GFP]*, **ZX2586**: *zxEx1228[punc-*
588 *17::GtACR2::mCerulean::βHK::Chrimson; pelt-2::GFP]*, **ZX2714**: *zxEx1250[punc-*
589 *17::GtACR2::mCerulean::βHK::Chrimson; pmyo-3::QuasAr2; pelt-2::GFP]*, **ZX2753**:
590 *zxEx1266[pmyo-3::GtACR2::mCerulean::βHK::Chrimson; pmyo-3::QuasAr2; pmyo-2::CFP]*,
591 **ZX2755**: *zxEx1268[punc-47::QuasAr2::GFP; pmyo-2::CFP]*, **ZX2826**: *zxEx1282[pmyo-*
592 *2::QuasAr2; pmyo-2::GtACR2::mCerulean::βHK::Chrimson; pmyo-3::CFP]*, **ZX2827**:
593 *zxEx1283[punc-17::GtACR2::mCerulean::βHK::Chrimson; punc-17::QuasAr2; pelt-2::GFP]*,
594 **ZX2828**: *zxEx1284[punc-47::QuasAr2::GFP; punc-47::GtACR2::mCerulean::βHK:: Chrimson;*
595 *pmyo-2::CFP]*, **ZX2876**: *zxIs139[pmyo-3::GtACR2::mCerulean::βHK::Chrimson; pmyo-*
596 *3::QuasAr2; pmyo-2::CFP]*, **ZX2935**: *unc-13(n2813)*; *zxIs139[pmyo-*
597 *3::GtACR2::mCerulean::βHK::Chrimson; pmyo-3::QuasAr2; pmyo-2::CFP]*.

598

599 **Molecular biology**

600 Plasmids pAB4 (p*unc-17*::ACR2::eYFP), pAB16 (p*myo-3*::QuasAr; Addgene plasmid #130272),
601 pAB17 (p*unc-17*::QuasAr), pAB23 (p*tdc-1s*::QuasAr::GFP) and pNH12 (p*myo-2*::MacQ::mCitrine)
602 were described earlier [19, 20]. **pAB26 (p*unc-17*::GtACR2::mCerulean::βHK::Chrimson)** was
603 generated by Gibson Assembly based on RM#348p (p*unc-17*; a gift from J. Rand) and pAAV-
604 hSyn-BiPOLES-mCerulean (Addgene plasmid #154944), using *Nhe*I and primers 5'-
605 attttcaggaggacccttggATGGCATCACAGGTCGTC-3' and 5'-
606 ataccatggtaccgtcgacgTCACACTGTGTCCTCGTC-3'. **pAB27 (p*myo-*
607 ***3*::GtACR2::mCerulean::βHK::Chrimson)** was generated *via* Gibson Assembly based on
608 pDD96.52 (p*myo-3*, Addgene plasmid #1608) and pAAV-hSyn-BiPOLES-mCerulean, using
609 *Bam*HI and primers 5'-actagatccatctagagATGGCATCACAGGTCGTC-3' and 5'-
610 ttggccaatcccgggCACTGTGTCCTCGTCCTC-3'. **pAB28 (p*unc-47*::QuasAr::GFP)** was
611 generated by Gibson Assembly based on pMSM08 (p*unc-47*::eGFP::MmBoNTB) and pAB23
612 (p*tdc-1s*::QuasAr::GFP), using *Xma*I, *Msc*I and primers 5'-
613 ttacagcaccggtggattggATGGTAAGTATCGCTCTG-3' and 5'-
614 ttctacgaatgctcctaggcCTATTTGTATAGTTCATCCATGC-3'. **pAB29 (p*myo-2*::QuasAr)** was
615 generated by Gibson Assembly based on pNH12 (p*myo-2*::MacQ::mCitrine) and pAB16 (p*myo-*

616 *3*::QuasAr), using primers 5'-caccgagtgaGAAGAGCAGGATCACCAG-3', 5'-
617 tgcagagcgatacttaccatCCCCGAGGGTTAAAATGAAAAG-3', 5'-ATGGTAAGTATCGCTCTGCAG-
618 3' and 5'-cctgctcttctcaCTCGGTGTCGCCCAGAATAG-3'. **pAB30 (p*myo-*
619 ***2*::GtACR2::mCerulean::bHK::Chrimson)** was generated by Gibson Assembly based on
620 pNH12 (p*myo-2*::MacQ::mCitrine) and pAAV-hSyn-BiPOLES-mCerulean, using *Bam*HI, *Hind*III
621 and primers 5'-ggacgaggacacagtgtgaaAAGAGCAGGATCACCAGC-3' and 5'-
622 agacgacctgtgatgccatgCCCCGAGGGTTAAAATGAAAAG-3'. **pAB31 (p*unc-*
623 ***47*::GtACR2::mCerulean::bHK::Chrimson)** was made by Gibson Assembly based on pAB28
624 (p*unc-47*::QuasAr::GFP) and pAAV-hSyn-BiPOLES-mCerulean, using *Age*I, *Eco*RI and primers
625 5'-acatttatttcattacagcaATGGCATCACAGGTCGTC-3' and 5'-
626 agcgaccggcgctcagttggTCACACTGTGTCCTCGTC-3'.
627 For neuronal expression, the coding sequence of QuasAr2 [49] (Addgene #107705) was cloned
628 together with a trafficking signal (ts: KSRITSEGEYIPLDQIDINV) and an ER-export signal (ER:
629 FCYENEV) from the Kir 2.1 channel [50, 51] into an AAV2-backbone behind a human synapsin
630 (hSyn) promoter resulting in **pAAV-QuasAr2-ts-ER.**
631
632 **OVC voltage imaging experiments**
633 For voltage imaging experiments, animals were supplemented with ATR (Sigma-Aldrich, USA):
634 One day prior to experiments, transgenic L4 stage animals were transferred to NGM plates,
635 seeded with OP50 bacterial suspension mixed with ATR (stock in ethanol). To avoid interfering
636 fluorescence of unbound ATR, its concentration was adjusted for each tissue. Final ATR
637 concentrations (mM): BWMs (0.01), pharynx (0.03), cholinergic neurons (0.1), GABAergic
638 neurons (0.005). Animals were immobilized with polystyrene beads (0.1 µm diameter, at 2.5 %
639 w/v, Sigma-Aldrich) on 10 % agarose pads (in M9 buffer). Voltage-dependent fluorescence of
640 QuasAr2 was excited with a 637 nm red laser (OBIS FP 637LX, Coherent) at 1.8 W/mm^2 and
641 imaged at 700 nm (700/75 ET Bandpass filter, integrated in Cy5 filter cube, AHF
642 Analysentechnik), while optogenetic actuators (BiPOLES, *Gt*ACR2 or ChR2(H134R)) were
643 activated using a monochromator (Polychrome V, Till Photonics / Thermo Scientific), set to emit
644 light from 400 to 600 nm at 300 µW/mm^2. Imaging was performed on an inverted microscope
645 (Zeiss Axio Observer Z1), equipped with a 40x oil immersion objective (Zeiss EC Plan-
646 NEOFLUAR 40x/ N.A. 1.3, Oil DIC ∞ / 0.17), a laser beam splitter (HC BS R594 lambda/2 PV flat,
647 AHF Analysentechnik), a galilean beam expander (BE02-05-A, Thorlabs) and an EMCCD or an
648 sCMOS camera (Evolve 512 Delta, Photometrics, or Kinetix 22, Teledyne). All OVC experiments
649 were performed at ≈ 90 fps with 10 ms exposure and a binning of 4x4 (computer specifications:
650 24 GB RAM, AMD FX-8150 Octa-core processor (3.6 GHz), NVIDIA GeForce GT 520). To induce

651 pharyngeal pumping, animals were incubated in 3 µl serotonin (20 mM, in M9) for 3 min prior to
652 experiments.
653
654 **OVC software**
655 The OVC control software was written in Beanshell, the scripting language used by the open
656 source microscopy software µManager v. 1.4.22 [34]. Scripts are provided in supplementary
657 information. Experiments were initiated via the µManager script panel. For support of Polychrome
658 V related commands, a copy of the Java archive file *TILLPolychrome.jar* must be placed into the
659 MMPlugins folder and the dynamic link library file *TILLPolychromeJ.dll* into the Sys32 folder (both
660 provided by Till Photonics). The OVC software is compatible with all cameras supported by
661 µManager. Before running the software, simple rectangular ROIs (to save computation capacity,
662 **Extended data Fig. 1B**) must be selected in the live image mode by using the ROI button in the
663 µManager main window. Once a ROI is selected, the script can be executed via the script panel
664 GUI. An input tab prompts the user to select the OVC- and acquisition parameters. The software
665 allows to define a holding $\Delta F/F_0$ value (in %) and the number of frames for each of the steps
666 (three-step-protocol). One can further select the number of frames for the calibration period, the
667 tolerance range (in %), the algebraic sign of the increment factor that decides whether to increase
668 or decrease the wavelength with respect to the current $\Delta F/F_0$, the starting wavelength and the
669 wavelength limits (in nm). The free choice of these parameters ensures that the program can also
670 be used for other and/or future combinations of optogenetic tools with different spectral properties.
671 For acquisition, light intensity of the Polychrome V (in %), exposure time of the camera (in ms)
672 and binning can be selected.
673 During calibration, acquired grey values are stored in an array and used to evaluate the
674 parameters for the exponential decay function to correct for bleaching of the voltage sensor, live
675 during the clamping phase (**Equation 1-3**; based on the ImageJ Plugin "Correctbleach" [52, 53]). At
676 the last time point of the calibration phase, the first 50 bleaching corrected gray values of the
677 recording are used to calculate F_0. Subsequently, bleaching corrected $\Delta F/F_0$ values are calculated
678 at each time point of the clamping phase (**Equation 4**). Once the system has access to the
679 bleaching-corrected $\Delta F/F_0$ values, it feeds them into a decision tree algorithm, where they are
680 compared to a desired holding $\Delta F/F_0$ value. Depending on the sign of the difference, it decides,
681 whether to shift the wavelength blue or red (mirrored by the sign of the increment i[k]). Wavelength
682 adaptation occurs *via* an implemented I-controller (integral gain K_I was empirically chosen to fit
683 the desired system-behavior) that maps the "I" dynamics by buffering the manipulated variable
684 (wavelength λ) to compensate for permanent control deviation, which would otherwise occur by
685 using a sole P-controller (**Extended data Fig. 1A**). That means that the difference (error) between

command and current $\Delta F/F_0$ determines the wavelength change of the monochromator – hence, the current wavelength results from the previous plus the respective wavelength change at each time point (**Equation 5 and 6**). The software comes with a three-step protocol, where among others, the desired holding values (within a tolerance range) and number of frames for each step can be selected by the user (**Extended data Fig. 1C**). The system changes the wavelength only if the tolerance range is exceeded.

$$exp.offset = a * e^{-b*frame} + c \quad \text{(Eq. 1)}$$

$$ratio = exp.offset_0 \div exp.offset_{frame} \quad \text{(Eq. 2)}$$

$$F_{correct} = F_{frame} * ratio \quad \text{(Eq. 3)}$$

$$\Delta F/F_{0_{correct}} = ((F_{correct} - F_0) / F_0) * 100 \quad \text{(Eq. 4)}$$

$$error = \left|\Delta F/F_{0_{holding}} - \Delta F/F_0\right| \quad \text{(Eq. 5)}$$

$$\lambda = \lambda_{frame-1} + K_I * error * increment \quad \text{(Eq. 6)}$$

Exp. offset: exponential offset. a, b, c: exponential fitting parameters. Ratio: ratio between first and current exponential offset. $F_{correct}$: Bleaching-corrected gray values. F_{frame}: Gray value of current frame. $\Delta F/F_{0_{correct}}$: Bleaching-corrected relative change in fluorescence. F_0: Resting fluorescence value. λ: wavelength. K_I: integral gain. Equations 1-3 based on the ImageJ Plugin "Correctbleach" [52].

When the OVC acquisition is complete, a results text file is given out, and the respective image stack is saved automatically as TIFF file. The results file comprises the selected parameters, the bleach correction function and its quality, the framerate, as well as time, (bleaching corrected-) raw grey- and $\Delta F/F_0$ values, and wavelength traces. In addition, status information (system on hold, adapting, or wavelength limits reached) is recorded for each time point of the clamp phase. For the "on-the-run" mode, an additional control window opens as soon as the measurement starts. Here, the holding $\Delta F/F_0$ values can be selected live, either via a range slider or with help of the keyboard arrow keys, while a live status update is displayed.

A further software version involves a PID-controller to adjust the wavelength of the OVC. At each time point, the new wavelength is calculated by the addition of the output (u) of the PID equation to the calibration wavelength (**Equations 7-9**).

$$error = \Delta F/F_{0_{holding}} - \Delta F/F_0 \quad \text{(Eq. 7)}$$

$$u = K_P * e + K_I * T_a * e_{sum} + K_D * \frac{e - e_{t-1}}{T_a} \quad \text{(Eq. 8)}$$

$$\lambda = \lambda_0 + u \quad \text{(Eq. 9)}$$

u: output. K_P: proportional gain. K_I: integral gain. K_D: derivative gain. e: error. T_a: sampling rate. e_{sum}: summed up error. λ_0: calibration wavelength.

Parameter tuning was performed by applying the Ziegler-Nichols method to empirically achieve system stability (**Extended data Fig. 2C**). Therefore, K_P was adapted until the system started to oscillate at the critical proportional gain ($K_{P\,crit}$). The oscillation period was noted as T_{crit}. PID coefficients were calculated according to **Equations 10 and 11**:

Ziegler-Nichols parameter tuning.

K_P	T_n	T_v
0.6 $K_{P\,crit}$	0.5 T_{crit}	0.12 T_{crit}

K_P: proportional gain. $K_{P\,crit}$: critical proportional gain. T_{crit}: period of oscillation. T_n: integration-coefficient. T_v: derivation-coefficient [35].

$$K_D = K_P * T_v \quad \text{(Eq. 10)}$$

$$K_I = K_P * \frac{1}{T_n} \quad \text{(Eq. 11)}$$

To also achieve a better controller performance, a Kalman filter for sensor smoothing was added (**Extended data Fig. 2A**). Here, the error covariances of the measurement- and system noise of the Kalman filter were empirically adjusted so that the OVC controller dynamics achieved a desired performance. After initializing the system state with an a priori estimate (variables $\hat{x}_0$: estimated fluorescence at the beginning of the measurement and P_0: estimated error covariance of measured fluorescence vs. estimated fluorescence at the beginning of the measurement), prediction and correction are performed at each time step, alternately propagating the system state in time, and correcting it with new observations (**Equations 12-17**) [54]:

1. Prediction of the fluorescence value and the error covariance:

$$x^*(k+1|k) = \mathbf{A}\hat{x}(k) \quad \text{(Eq. 12)}$$

$$\mathbf{P}^*(k+1|k) = \mathbf{A}\mathbf{P}(k)\mathbf{A}^\top + \mathbf{Q} \quad \text{(Eq. 13)}$$

k: discrete time-Step. A: system matrix, was here set to scalar value one (which is sufficient for error smoothing). x^*: predicted fluorescence. P^*: predicted error covariance of the estimate. Q: Error covariance of the system noise. $\mathrm{P}(k)$: estimated error covariance.

2. Calculation of the Kalman gain:

$$\mathbf{S}(k+1) = \mathbf{H}\mathbf{P}^*(k+1|k)\mathbf{H}^\top + \mathbf{R} \quad \text{(Eq. 14)}$$

$$\mathbf{K}(k+1) = \mathbf{P}^*(k+1|k)\mathbf{H}^\top\mathbf{S}^{-1}(k+1) \quad \text{(Eq. 15)}$$

S: auxiliary quantity for determining the Kalman gain. H: system output matrix. R: error covariance matrix of the measurement noise. K: Kalman gain.

3. Correction of the state estimate:

$$\hat{x}(k+1) = x^*(k+1|k) + \mathbf{K}(k+1)[z(k+1) - \mathbf{H}x^*(k+1|k)] \quad \text{(Eq. 16)}$$

$z(k+1)$: current measurement. $x^*(k+1|k)$: predicted measurement. $\hat{x}(k+1)$: current estimate.

4. Correction of the covariance estimation

$$\mathbf{P}(k+1) = [\mathbb{1} - \mathbf{K}(k+1)\mathbf{H}]\mathbf{P}^*(k+1|k) \qquad \text{(Eq. 17)}$$

The system matrices A and H were set as constant scalars (A = 1, H = 1; constant system dynamics) since this assumption is perfectly sufficient for signal smoothing for the PID controller. Here, the sampling rate is fast enough that the Kalman filter can respond to membrane potential changes occurring in this time period with reasonable estimates.

Quality assessment of the OVC

The predictive accuracy for bleaching correction had R^2 values above 0.95 in most cases, and at least above 0.8 (**Extended data Fig. 6B**). Experiments with lower R^2 values were attributable to APs occurring during the calibration phase (e.g. in pharyngeal muscle). As expected, the fraction of system saturation decreased once optogenetic tools for de- and hyperpolarization were simultaneously used, which stresses the importance of a second, opposing actuator (**Extended data Fig. 6C**). While for the single-tool approaches, the percentage of system saturation was relatively high with 16.3 ± 2.8 %, this relation was significantly reduced for all bidirectional BiPOLES combinations. This was also reflected in the speed of the system, where compared to single-tool combinations, BiPOLES was significantly faster, particularly for driving excited or hyperpolarized states back towards resting potential (**Extended data Fig. 6A**).

Electrophysiology in *C. elegans*

Electrophysiological recordings from body wall muscle cells were conducted in immobilized and dissected adult worms as described previously [40]. Animals were immobilized with Histoacryl L glue (B. Braun Surgical, Spain) and a lateral incision was made to access neuromuscular junctions (NMJs) along the anterior ventral nerve cord. The basement membrane overlying body wall muscles was enzymatically removed by 0.5 mg/ml collagenase for 10 s (C5138, Sigma-Aldrich, Germany). Integrity of BWMs and nerve cord was visually examined *via* DIC microscopy. Recordings from BWMs were acquired in whole-cell patch-clamp mode at 20-22°C using an EPC-10 amplifier equipped with Patchmaster software (HEKA, Germany).

The head stage was connected to a standard HEKA pipette holder for fire-polished borosilicate pipettes (1B100F-4, Worcester Polytechnic Institute, Worcester, MA, USA) of 4-10 MΩ resistance. The extracellular bath solution consisted of 150 mM NaCl, 5 mM KCl, 5 mM $CaCl_2$, 1 mM $MgCl_2$, 10 mM glucose, 5 mM sucrose, and 15 mM HEPES (pH 7.3 with NaOH, ≈330 mOsm). The internal/patch pipette solution consisted of K-gluconate 115 mM, KCl 25 mM, $CaCl_2$ 0.1 mM, $MgCl_2$ 5 mM, BAPTA 1 mM, HEPES 10 mM, Na_2ATP 5 mM, Na_2GTP 0.5 mM, cAMP 0.5 mM, and

784 cGMP 0.5 mM (pH 7.2 with KOH, ≈320 mOsm). For some experiments, BAPTA was replaced by
785 EGTA (5 mM).
786 For light activation a monochromator (Polychrome V, Thermo Scientific) was used, ranging from
787 400 to 600 nm at 300 µW/mm^2. To create conditions as similar as possible to those for the OVC
788 experiments, additional excitation was performed with a laser at 637 nm. Subsequent analysis
789 and graphing were performed using Patchmaster, and Origin (Originlabs).
790 Electrophysiological recordings from the DVB neuron were conducted in immobilized and
791 dissected adult worms as described previously [44] with minor modifications. Both dissection and
792 recording were performed at room temperature. Briefly, an animal was immobilized with
793 cyanoacrylate adhesive (Vetbond tissue adhesive; 3M) along the ventral side of the posterior
794 body on a Sylgard 184-coated (Dow Corning) glass coverslip. A small longitudinal incision was
795 made using a diamond dissecting blade (Type M-DL 72029 L; EMS) in the tail region along the
796 glue line. The cuticle flap was folded back and glued to the coverslip with GLUture Topical
797 Adhesive (Abbott Laboratories), exposing DVB. The coverslip with the dissected preparation was
798 then placed into a custom-made open recording chamber (~1.5 ml volume) and treated with 1
799 mg/ml collagenase (type IV; Sigma) for ~10 s by hand pipetting. The recording chamber was
800 subsequently perfused with the standard extracellular solution using a custom-made gravity-feed
801 perfusion system for ~10 ml. The standard pipette solution was (all concentrations in mM): K-
802 gluconate 115; KCl 15; KOH 10; $MgCl_2$ 5; $CaCl_2$ 0.1; Na_2ATP 5; NaGTP 0.5; Na-cGMP 0.5; cAMP
803 0.5; BAPTA 1; Hepes 10; Sucrose 50, with pH adjusted to 7.2, using KOH, osmolarity 320–330
804 mOsm. The standard extracellular solution was: NaCl 140; NaOH 5; KCl 5; $CaCl_2$ 2; $MgCl_2$ 5;
805 Sucrose 15; Hepes 15; Dextrose 25, with pH adjusted to 7.3, using NaOH, osmolarity 330–340
806 mOsm. Liquid junction potentials were calculated and corrected before recording. Electrodes with
807 resistance of 20–30 MΩ were made from borosilicate glass (BF100-58-10; Sutter Instruments)
808 using a laser pipette puller (P-2000; Sutter Instruments) and fire-polished with a microforge (MF-
809 830; Narishige). Recordings were performed using single-electrode whole-cell current-clamp
810 (Heka, EPC-10 USB) with two-stage capacitive compensation optimized at rest, and series
811 resistance compensated to 50 %.
812
813 **Preparation of organotypic hippocampal slice cultures and transgene delivery**
814 All procedures were in agreement with the German national animal care guidelines and approved
815 by the independent Hamburg state authority for animal welfare (Behörde für Justiz und
816 Verbraucherschutz). They were performed in accordance with the guidelines of the German
817 Animal Protection Law and the animal welfare officer of the University Medical Center Hamburg-
818 Eppendorf.

819 Organotypic hippocampal slices were prepared from Wistar rats of both sexes (Jackson-No.
820 031628) at post-natal day 5-7 as previously described [55]. In brief, dissected hippocampi were cut
821 into 350 µm slices with a tissue chopper and placed on a porous membrane (Millicell CM,
822 Millipore). Cultures were maintained at 37°C, 5% CO_2 in a medium containing 80% MEM (Sigma
823 M7278), 20% heat-inactivated horse serum (Sigma H1138) supplemented with 1 mM L-glutamine,
824 0.00125% ascorbic acid, 0.01 mg ml^{-1} insulin, 1.44 mM $CaCl_2$, 2 mM $MgSO_4$ and 13 mM D-
825 glucose. No antibiotics were added to the culture medium. Pre-warmed medium was replaced
826 twice per week.
827 For transgene delivery, organotypic slice cultures were transduced at DIV 3-5 with a recombinant
828 adeno-associated viral vector (rAAV) encoding a soma-targeted version of BiPOLES [26] (AAV9-
829 CaMKII-somBiPOLES-mCerulean, Addgene #154948). The rAAV was locally injected into the
830 CA1 region using a Picospritzer (Parker, Hannafin) by a pressurized air pulse (2 bar, 100 ms)
831 expelling the viral suspension into the slice [56]. During virus transduction, membranes carrying the
832 slices were kept on pre-warmed HEPES-buffered solution. At DIV 14-16, individual CA1 pyramidal
833 cells in the previously somBiPOLES-transduced slices were transfected by single-cell
834 electroporation [57] with the plasmid pAAV-QuasAr2-ts-ER at a final concentration of 10 ng/µl in K-
835 gluconate-based solution consisting of (in mM): 135 K-gluconate, 10 HEPES, 4 Na_2-ATP, 0.4 Na-
836 GTP, 4 $MgCl_2$, 3 ascorbate, 10 Na_2- phosphocreatine (pH 7.2). An Axoporator 800A (Molecular
837 Devices) was used to deliver 50 hyperpolarizing pulses (-12 V, 0.5 ms) at 50 Hz. During
838 electroporation slices were maintained in pre-warmed (37°C) HEPES-buffered solution (in mM):
839 145 NaCl, 10 HEPES, 25 D-glucose, 2.5 KCl, 1 $MgCl_2$ and 2 $CaCl_2$ (pH 7.4, sterile filtered). A
840 plasmid encoding hSyn-mCerulean (at 50 ng/µl) was co-electroporated and served as a marker
841 to rapidly identify cells putatively co-expressing QuasAr2 and somBiPOLES under
842 epifluorescence excitation.
843
844 **OVC voltage imaging and electrophysiology experiments in rat organotypic slices**
845 At DIV 19-21, voltage imaging and/or whole-cell patch-clamp recordings of transfected CA1
846 pyramidal neurons were performed. Experiments were done at room temperature (21-23°C) using
847 a BX51WI upright microscope (Olympus) equipped with an EMCCD camera (Evolve 512 Delta,
848 Photometrics), dodt-gradient contrast and a Double IPA integrated patch amplifier controlled with
849 SutterPatch software (Sutter Instrument). QuasAr2 was excited with a 637 nm red laser (OBIS
850 FP 637LX, Coherent) at 0.52 W/mm^2 via a dichroic mirror (660nm, Edmund Optics) and voltage-
851 dependent fluorescence was detected through the objective LUMPLFLN 60XW (Olympus) and
852 through an emission filter (732/68 nm Bandpass filter, Edmund Optics). somBiPOLES was
853 activated using a monochromator (Polychrome V, Till Photonics / Thermo Scientific), set to emit

854 light from 400 to 600 nm at 1.7 mW/mm^2. Laser and monochromator light were combined using
855 a 605nm dichroic mirror (Edmund Optics). Irradiance was measured in the object plane with a
856 PM400 power meter equipped with a S130C photodiode sensor (Thorlabs) and divided by the
857 illuminated field of the Olympus LUMPLFLN 60XW objective (0.134 mm^2). As for *C.elegans*, OVC
858 experiments were performed at ≈ 90 fps with 10 ms exposure and a binning of 4x4.
859 For electrophysiology, patch pipettes with a tip resistance of 3-4 MOhm were filled with
860 intracellular solution consisting of (in mM): 135 K-gluconate, 4 $MgCl_2$, 4 Na_2-ATP, 0.4 Na-GTP,
861 10 Na_2-phosphocreatine, 3 ascorbate, 0.2 EGTA, and 10 HEPES (pH 7.2). Artificial cerebrospinal
862 fluid (ACSF) consisted of (in mM): 135 NaCl, 2.5 KCl, 2 $CaCl_2$, 1 $MgCl_2$, 10 Na-HEPES, 12.5 D-
863 glucose, 1.25 NaH_2PO_4 (pH 7.4). Synaptic transmission was blocked by adding 10 µM CPPene,
864 10 µM NBQX, and 100 µM picrotoxin (Tocris) to the extracellular solution. Measurements were
865 corrected for a liquid junction potential of -14,5 mV. Access resistance of the recorded neurons
866 was continuously monitored and recordings above 30 MΩ were discarded.
867
868 **Statistical methods**
869 Statistical methods used are described in the figure legends. No sample was measured multiple
870 times, and no samples were excluded from analysis. Statistical analysis was performed in Prism
871 (Version 8.0.2, GraphPad Software, Inc.), OriginPro 2021 (OriginLab Corporation, Northampton,
872 USA), Microsoft Excel 2016, 2019, SutterPatch V2 (Sutter Instrument) MATLAB 2016b, 2019b
873 (Mathworks), or ImageJ v1.53c. No statistical methods were applied to predetermine sample size.
874 However, sample sizes reported here are consistent to data presented in previous publications,
875 and which typically allow distinction of significant differences in the types of experiments used.
876 Data was tested for normality prior to statistical inference. Data is given as means ± SEM, if not
877 otherwise stated. Significance between data sets after paired or two-sided t-test or ANOVA, with
878 Bonferroni correction for multiple comparisons, is given as p-value (* $p \leq 0.05$; ** $p \leq 0.01$; *** $p \leq$
879 0.001), when not otherwise stated. Group data are presented as box plots with median (line), 25-
880 75th quartiles (box), mean (open dot) and whiskers, representing 1.5x inter quartile range (IQR).
881 Single data points are shown for n≤10. The R^2 coefficient of determination was determined as: R^2
882 = 1 - SSE/SSD (SSE = sum of the squared errors; SSD = sum of the squared deviations about
883 the mean).

Extended data

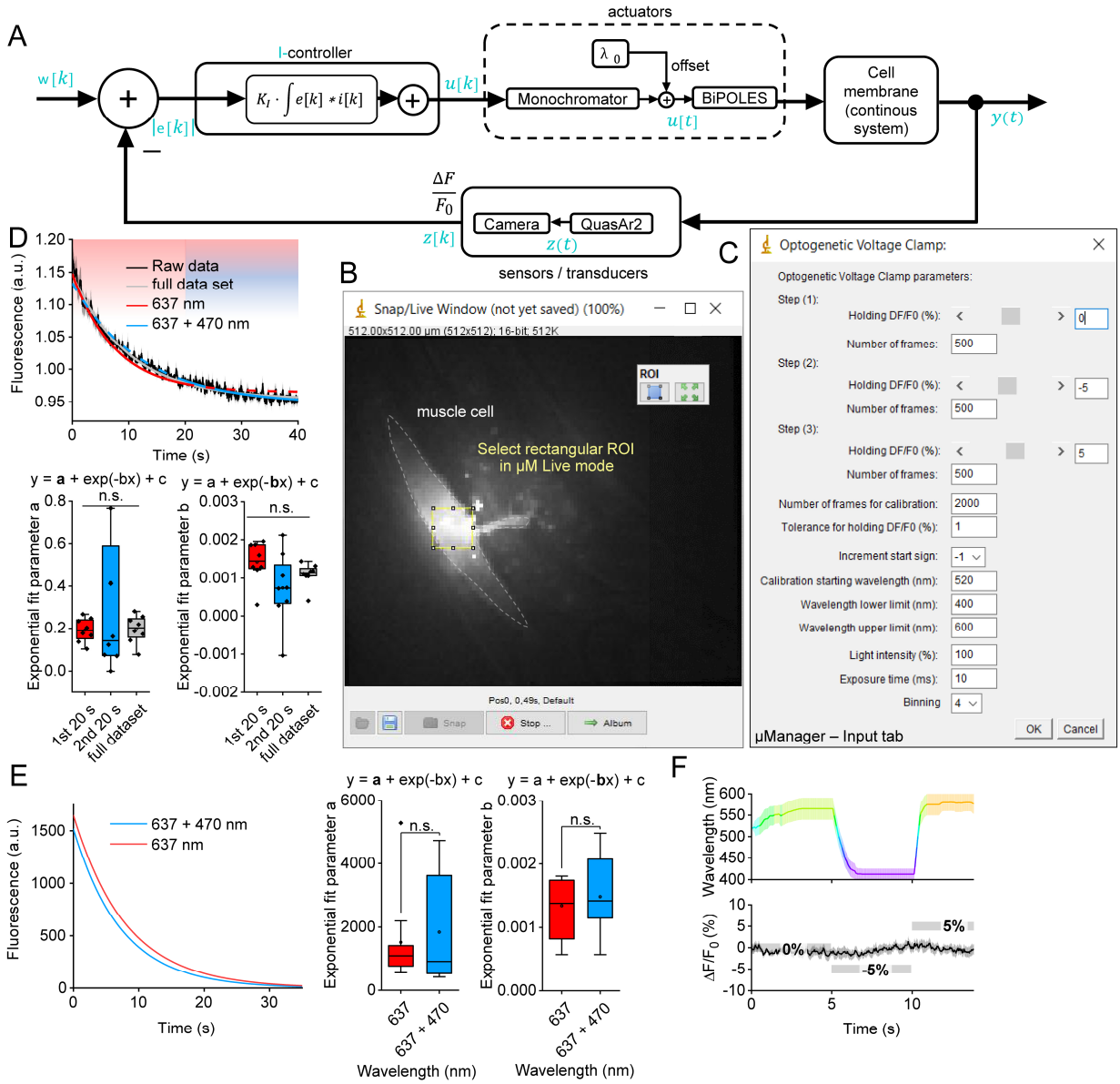

Extended data Figure 1. Setup of the OVC software and control parameters. (A) Wiring diagram of I-controller: I-controller generates a digital control value u[k] based on error e[k] for the monochromator, which in turn generates analog light output u[t]. BiPOLES modulates membrane voltage y(t) upon analog light activation that in turn defines QuasAr2's fluorescence z(t) (transduced analog actual value). Fluorescence is monitored via camera and $\Delta F/F_0$ is calculated (digital actual value). w[k]: Set point. **(B)** Rectangular ROI selection in µManager "live mode" prior to OVC measurement. **(C)** Input tab of the standard OVC software, implemented in µManager. **(D)** Bleaching behavior and exponential fits of the fluorescence of QuasAr2 in BWMs, in control animals expressing no actuators. Animals were illuminated with the 637 nm laser for the entire duration, and in addition, with 470 nm (300 µW/mm^2) for the last 20 s (n = 8). Fits were performed for the first (red) or second 20 sec period (blue), or for the entire duration (grey). Lower panel: Statistical analysis of the deduced fit parameters (n = 9). **(E)** Exponential fits of QuasAr2 fluorescence as in (D) but illuminated with either 637 nm laser or 637 nm laser and 470 (300 µW/mm^2) for the entire duration. Middle and right

panels: Statistical analysis of the fit parameters of data in left panel (n = 11-12). **(F)** Average data for animals expressing only QuasAr2 in BWMs, while the OVC attempts to run a 0, -5, 5 % $\Delta F/F_0$ protocol (n = 8). Upper panel: Monochromator wavelength; lower panel: mean fluorescence traces. Statistically significant differences analyzed by One-way ANOVA or two-sided t-test with Bonferroni correction (in D, E). Box plots (median, 25-75th quartiles); mean: open dot; whiskers: 1.5x inter-quartile range (IQR).

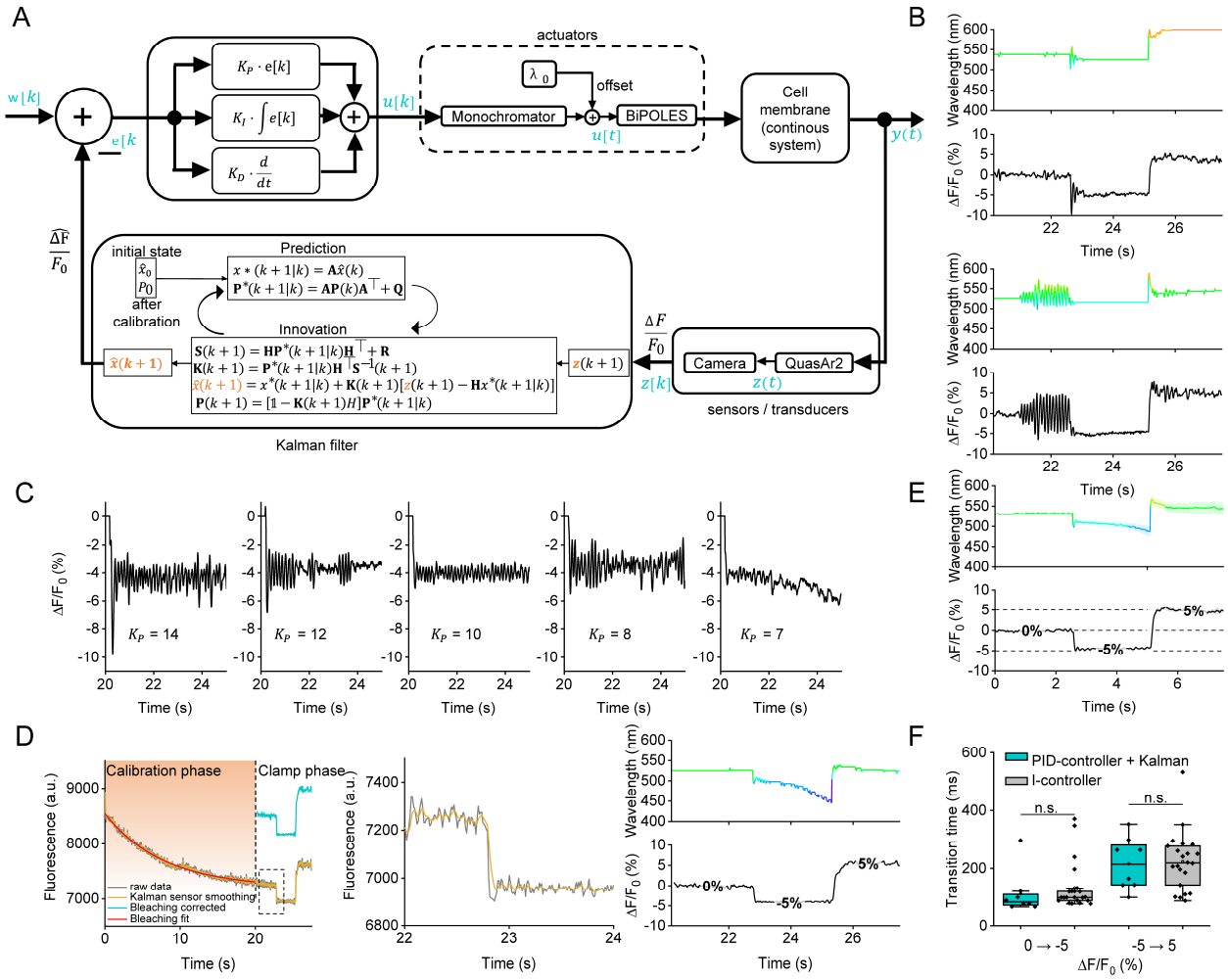

Extended data Figure 2. Implementation of a PID controller with Kalman filter. (A) Wiring diagram of PID-controller with Kalman filter. Signal flow as in Fig. S1A with the addition of a Kalman filter. **(B)** Comparison of single OVC experiments with PID control but without Kalman filter. **(C)** Ziegler-Nichols parameter tuning. **(D)** OVC three-step protocol (0, -5 and 5 % $\Delta F/F_0$) in BWMs, insets for close-up. Wavelength shown in the respective color, holding values are indicated for each step, yellow trace represents data processed with Kalman filter for sensor smoothing. Orange shade in left panel: transition period to reach tolerance range. **(E)** Upper panel: Overlay of mean (± S.E.M.) wavelength and (lower panel) fluorescence traces (n=8; holding values: 0, -5, 5 % $\Delta F/F_0$). **(F)** Times required for the indicated 5 and 10 % $\Delta F/F_0$ transitions for PID- (plus Kalman filter) and I-controller (n=8-22). Statistically significant differences analyzed by Two-sided t-test with Bonferroni correction. Box plots (median, 25-75th quartiles); mean: open dot; whiskers: 1.5x inter-quartile range (IQR).

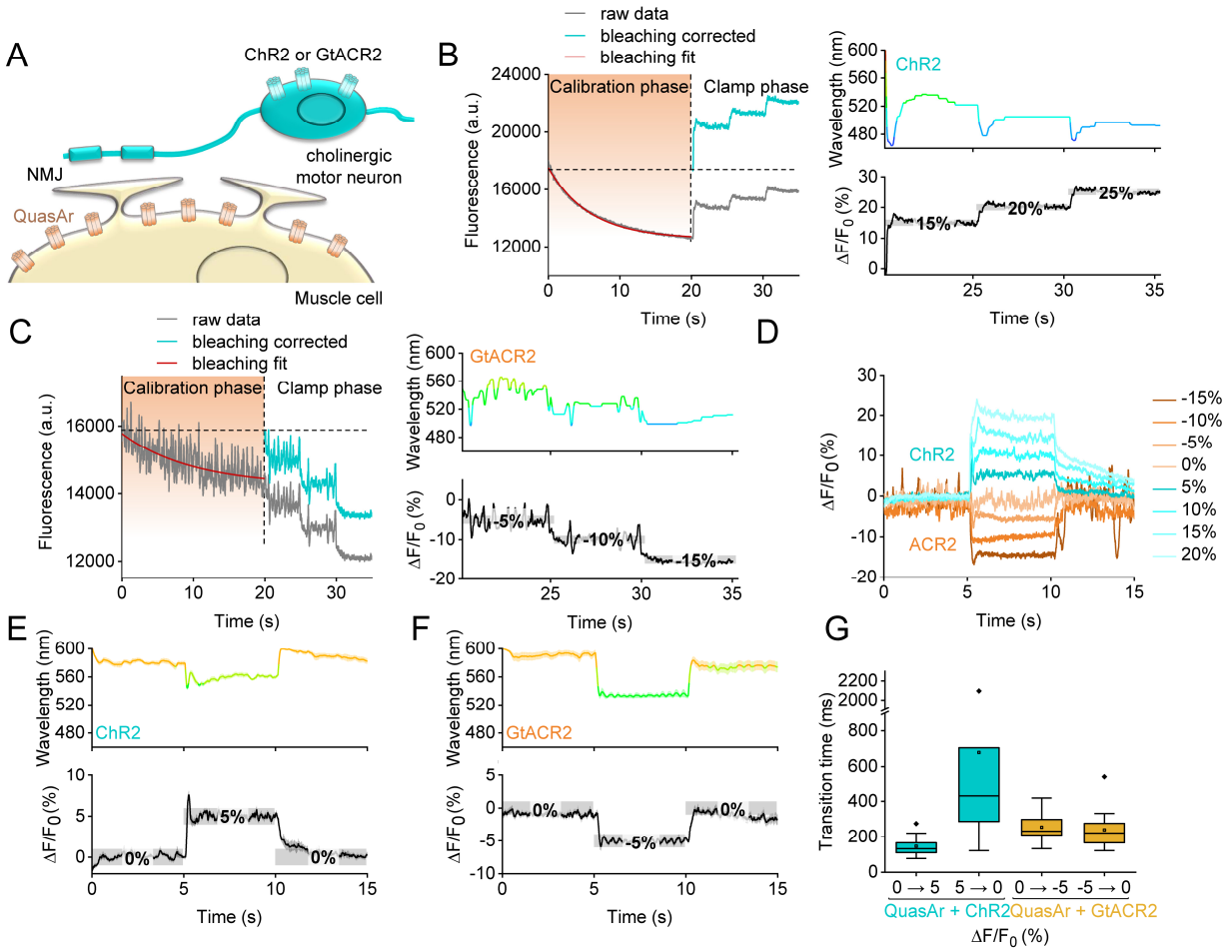

Extended data Figure 3. Unidirectional steering of membrane voltage. (A) Cholinergic neurons express either ChR2 or *Gt*ACR2, while QuasAr2 is expressed in BWMs. **(B)** Three-step protocol in ChR2 animals. Left: Raw and bleaching corrected data of calibration (red: exponential fit) and clamping phase. Right panels: Corresponding wavelength and $\Delta F/F_0$ traces. Holding values 15, 20 and 25 % $\Delta F/F_0$; grey shade: tolerance range for each step. **(C)** Three-step (-5, -10 and -15 % $\Delta F/F_0$) protocol in *Gt*ACR2 animals, as in (B). **(D)** Single traces for both strains, 0 %, then -15 to 20 % $\Delta F/F_0$ (in 5% increments), and return to baseline. **(E)** Mean (± S.E.M.) traces (n = 17); holding values: 0, 5, 0 % $\Delta F/F_0$, in ChR2 animals. **(F)** As in E, for *Gt*ACR2 animals (n = 14; 0, -5, 0 % $\Delta F/F_0$). **(G)** Transition time, respective 5 % $\Delta F/F_0$ steps; box plots (median, 25-75th quartiles); mean: open dot; whiskers: 1.5x inter-quartile range (IQR).

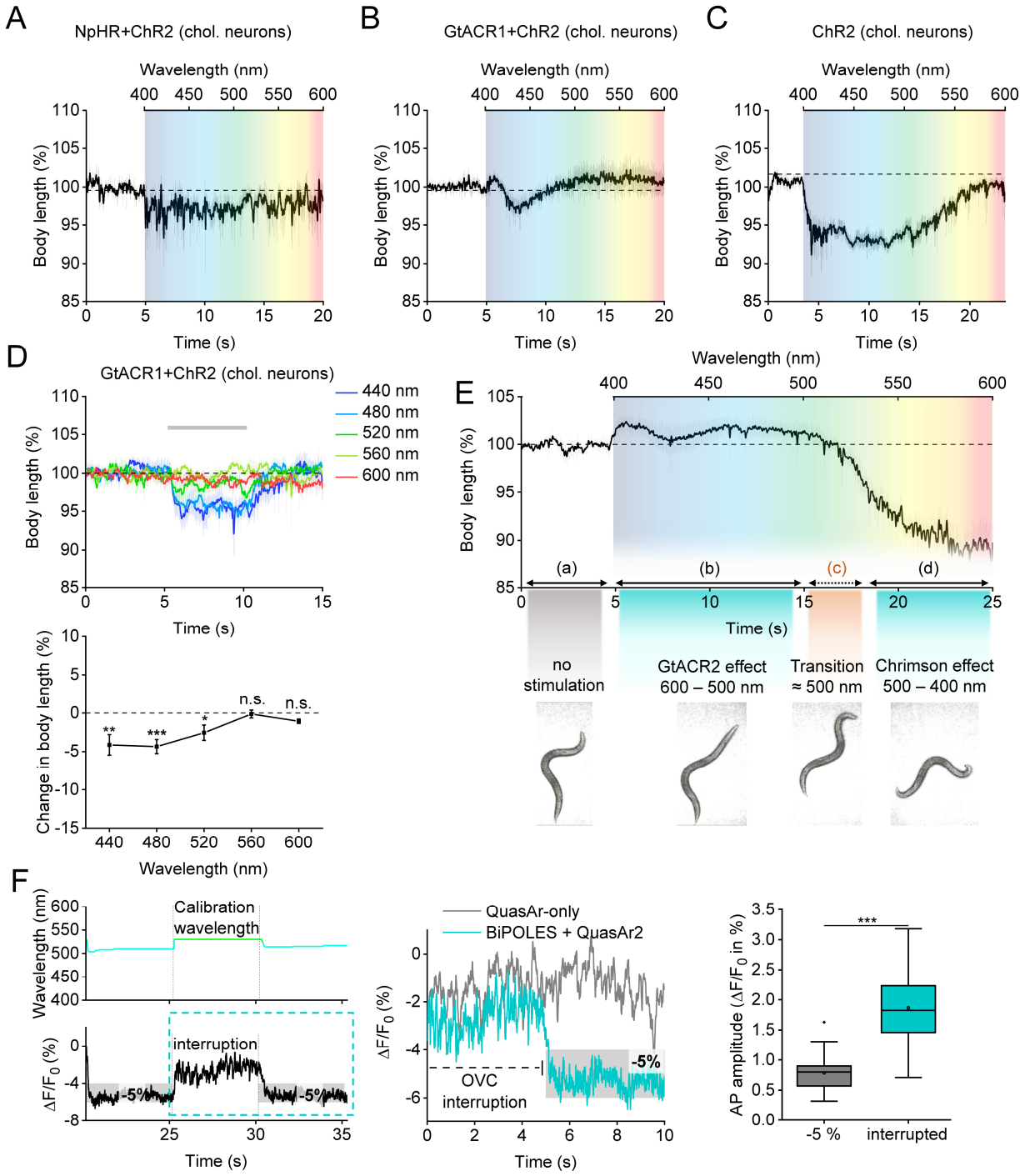

Extended data Figure 4. Testing different combinations of depolarizing and hyperpolarizing actuators. (A-E) Body length measurements to test functionality of optogenetic actuator combinations, expressed in cholinergic neurons. (A) NpHR and ChR2 (n = 8, monochromator wavelength ramp from 400 to 600 nm, 300 µW/mm^2). (B) *Gt*ACR1 and ChR2 (n = 10). (C) ChR2-only (n = 8). (D) *Gt*ACR1 and ChR2. Upper panel: 5 s light pulses, wavelength as indicated, 300 µW/mm^2 (n = 5-7). Lower panel: Mean (± S.E.M.) body length changes. Statistically significant differences were analyzed by one-way ANOVA with Bonferroni correction (***P ≤ 0.001, **P ≤ 0.01, *P ≤ 0.05). (E) Upper panel: Body length measurements of animals expressing BiPOLES in cholinergic neurons (mean ± S.E.M., wavelength ramp 400 -

600 nm, n = 8). Below: Representative still images of animals for each phase of the experiment: (a) before light, (b) *Gt*ACR2 effect / muscle relaxation, (c) transition from hyper- to depolarization, (d) Chrimson effect / muscle contraction. **(F)** Left panel: OVC experiment in BWMs (BiPOLES and QuasAr2) with clamp interruption (protocol: 1) holding value -5 %, wavelength determined by OVC, 2) interruption at calibration wavelength, 3) holding value - 5 % $\Delta F/F_0$). Middle panel: Close-up, with comparison to voltage fluorescence activity of unstimulated animals expressing only QuasAr2. Right panel: Group data of $\Delta F/F_0$ fluorescence amplitudes of typical, action potential-based fluctuations during -5 % clamping and no OVC action, as well as in animals expressing only QuasAr (n=30). Box plots (median, 25-75th quartiles); mean: open dot; whiskers: 1.5x inter-quartile range (IQR).

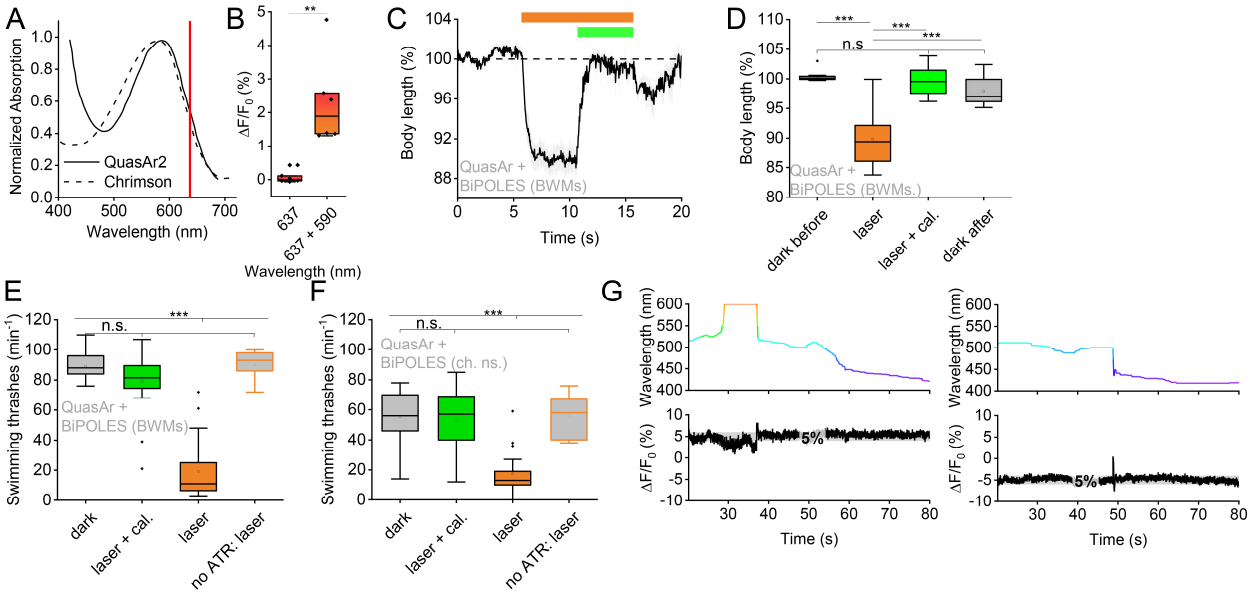

Extended data Figure 5. BiPOLES activation by 637 nm laser light and calibration wavelength have no adverse effects on muscle function and locomotion. (A) Normalized absorption spectra of Chrimson and QuasAr2 [25, 38], laser wavelength used for QuasAr2 imaging is indicated by a red line. **(B)** Mean $\Delta F/F_0$ QuasAr2 signal (n=6) in BWMs (co-expressed with BiPOLES) in the presence of laser light (637 nm) and additional signal in response to Chrimson excitation light (590 nm). **(C)** Body length measurements of animals expressing BiPOLES and Quasar in BWMs (mean ± S.E.M., light pulses: 637 nm laser and 637 nm laser plus calibration wavelength (ca. 521 nm), n = 14). **(D)** Statistical analysis of data in (C). **(E, F)** Analysis of swimming activity of animals expressing BiPOLES and Quasar in BWMs (E, n = 9-20) or cholinergic neurons (F, n = 10-18). Illumination parameters as in (D), or in the absence of all-*trans* retinal (ATR). In (D, E, and F): Statistically significant differences were analyzed by two-sided t-test or One-way ANOVA with Bonferroni correction (***P ≤ 0.001, **P ≤ 0.01, *P ≤ 0.05). In (B, D, E, and F): Box plots (median, 25-75th quartiles); mean: open dot; whiskers: 1.5x inter-quartile range (IQR). **(G)** Two examples of long-term OVC experiments (BWMs: BiPOLES and QuasAr2, holding values 5 and -5 % $\Delta F/F_0$).

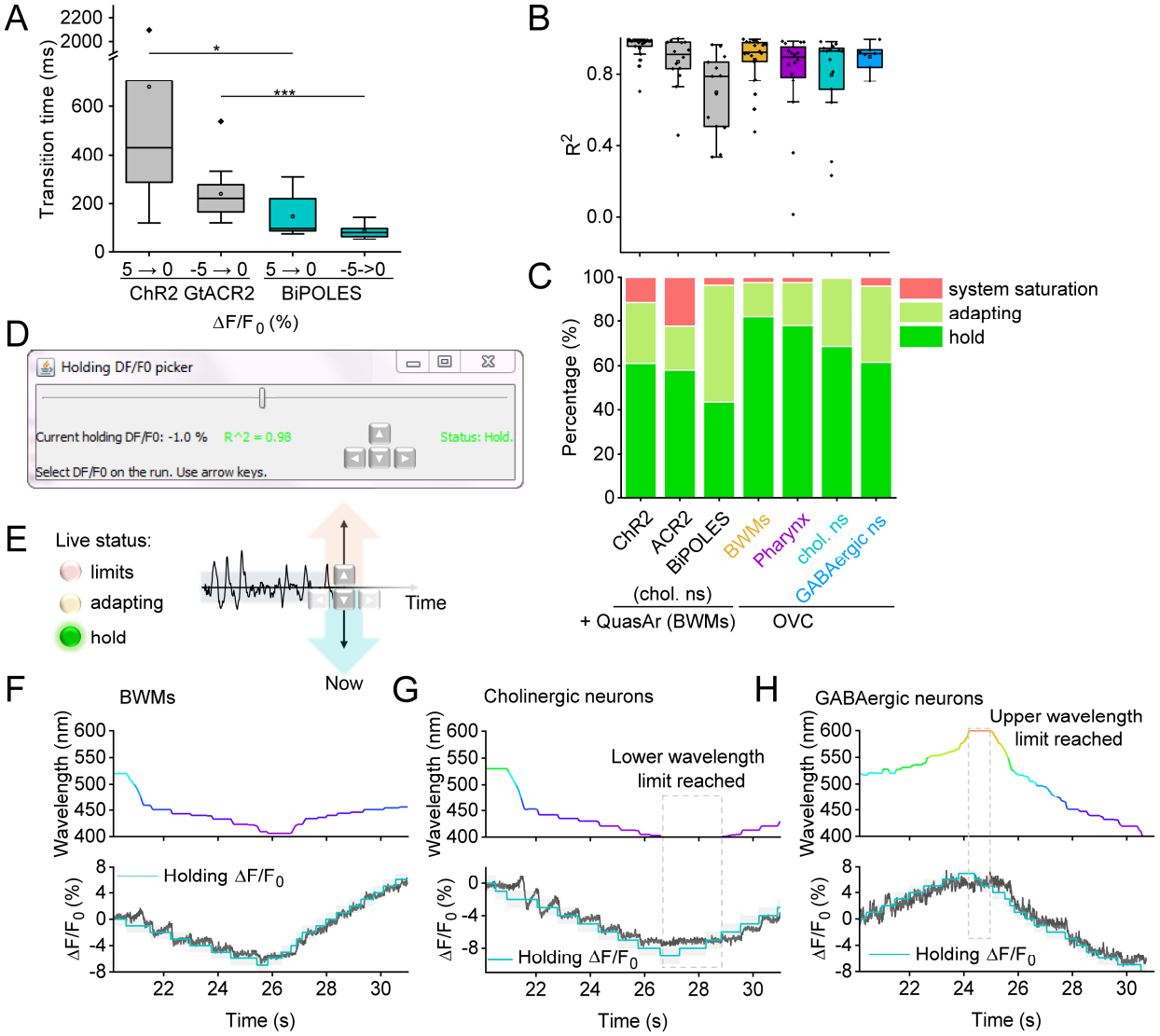

Extended data Figure 6. Performance assessment of the OVC and software version for live voltage adjustment. **(A)** Summary of OVC speed, reflected by the time needed for a 5 % $\Delta F/F_0$ step for different configurations (single tools, same-cell approach; n=10-22). **(B)** Quality of the exponential fit for bleach correction (coefficient of determination, R^2), for the different QuasAr2 / optogenetic actuator combinations, as indicated (n=7-22). **(C)** Percentages of the clamping status (hold, adapting, system saturation), for the different QuasAr2 / optogenetic actuator combinations, as indicated (n=7-22). **(D-H)** Time-varying OVC live control. (D) User interface for software version allowing live control of membrane voltage fluorescence. (E) Scheme: Holding values can be selected using arrow keys. Live status (system on hold, adapting or exceeding limits) is shown, enabling adjustment. (F-H) Example traces of wavelength (upper panels) and holding values as % $\Delta F/F_0$ (lower panels) in BWMs (F) cholinergic (G) and GABAergic neurons (H). Statistically significant differences were analyzed by one-way ANOVA with Bonferroni correction (***P ≤ 0.001, **P ≤ 0.01, *P ≤ 0.05). Box plots (median, 25-75th quartiles); mean: open dot; whiskers: 1.5x inter-quartile range (IQR).

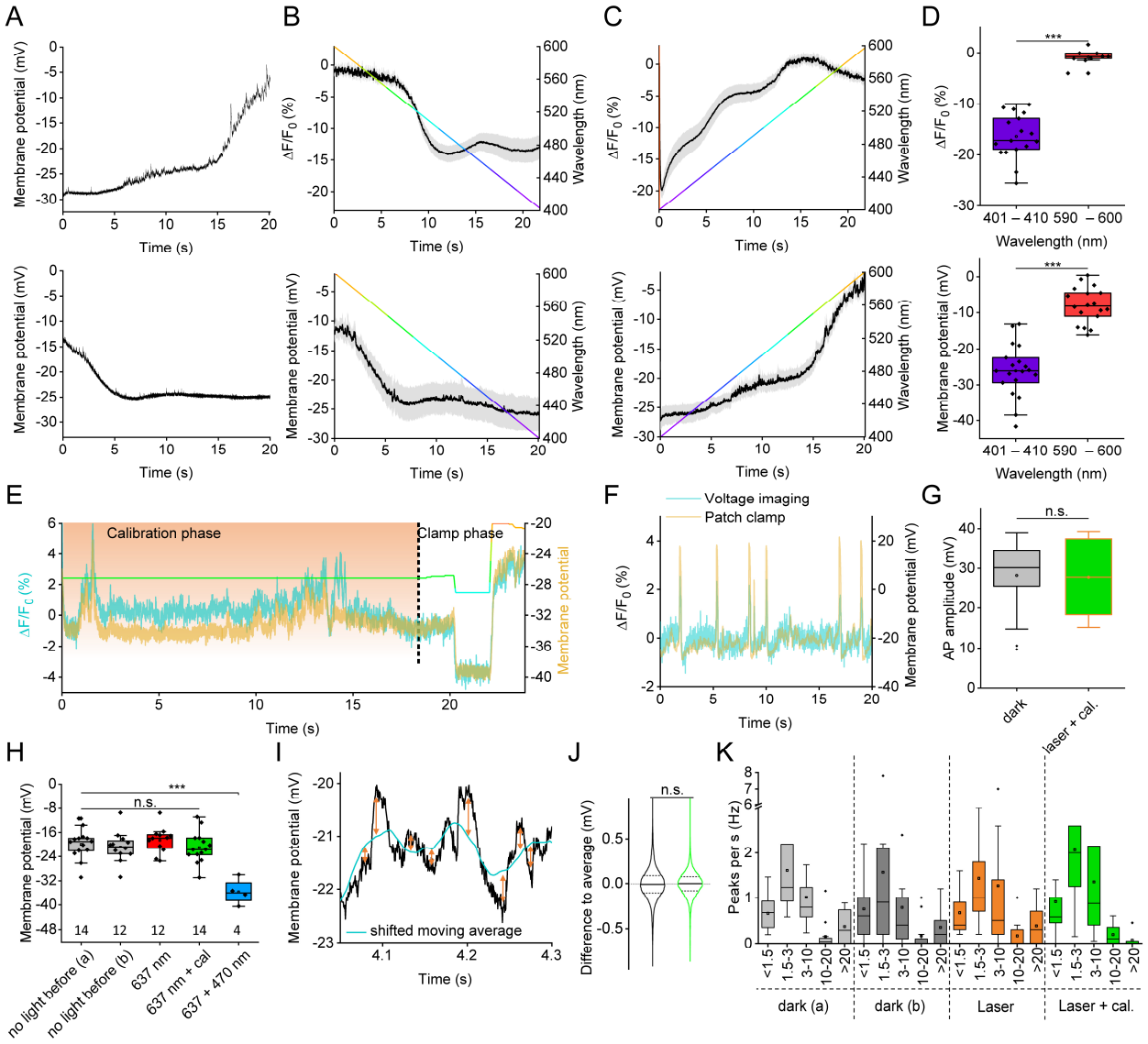

Extended data Figure 7. Calibrating voltage and fluorescence, and normal membrane voltage behavior in BiPOLES-activated BWMs. (A-C) Calibration of fluorescence (upper panels, n=9) and voltage in BWMs (lower panels, n = 8), corresponding to wavelength ramps from 600-400 nm (B) or 600-400 nm (C), with simultaneous 637 nm laser excitation. Changes in QuasAr2 fluorescence ($\Delta F/F_0$) shown as mean (± S.E.M.), and membrane potential was recorded in whole-cell patch-clamp mode. Single voltage traces are presented in (A). **(D)** Mean relative fluorescence change, or membrane potential (between 401-410 and 590-600 nm), upper and lower panels, respectively. **(E)** Original record of simultaneous voltage and fluorescence measurement during calibration and clamp phase (3 step OVC protocol, -3, +3 % $\Delta F/F_0$). Note the fluorescence trace was subsequently bleaching-corrected for the calibration phase. **(F)** APs in simultaneous patch-clamp and fluorescence recordings during OVC calibration phase (637 nm laser and 521 nm calibration wavelength). **(G)** Statistical analysis of AP amplitude. N = 4 recordings, n = 24-27 APs. **(H)** Membrane potential in muscle was measured by patch-clamp under the indicated light conditions. **(I, J)** Analysis of small, subthreshold voltage fluctuations observed during patch-clamp, without or with 637 nm laser and calibration wavelength. Differences (arrows) of actual peaks to shifted moving average (blue), as a proxy for base line (I), were statistically analyzed in (J). n=14 recordings, with ca. 55.000 single data points per measurement. **(K)** Frequency distribution of distinct voltage signals, incl. APs, observed during patch-clamp recordings. Mean number of events

(+S.E.M.) per second is shown as a function of peak amplitudes (in mV), for the different illumination conditions, as indicated below. N = 14, n = 3118 peaks. None of the respective amplitude distributions showed significant differences to any other bins. Statistically significant differences were analyzed by one-way ANOVA with Bonferroni correction (in H, J) or paired, two-sided t-test (in I). Box plots (median, 25-75th quartiles); mean: open dot; whiskers: 1.5x inter-quartile range (IQR).

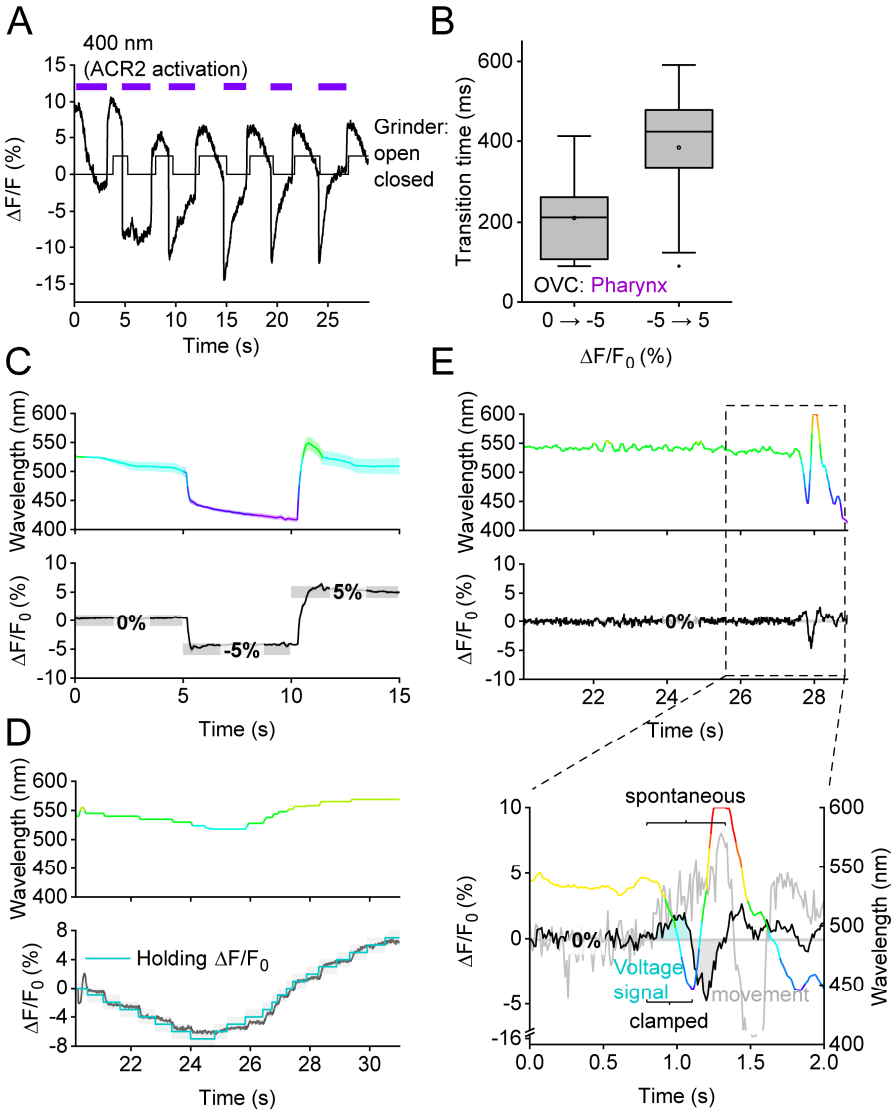

Extended data Figure 8. Voltage imaging and OVC measurements in pharyngeal muscle and the motor neuron DVB. (A) Voltage imaging and analysis of grinder opening in animals expressing QuasAr2 and BiPOLES in pharyngeal muscle, stimulated with consecutive 400 nm light pulses (300 µW/mm^2). Corresponding open or closed state of the grinder as indicated. **(B)** Transition time required by the OVC in the pharynx to execute 5 and 10 % $\Delta F/F_0$ steps. **(C)** Mean (± S.E.M.) traces (n = 16) of OVC protocol in pharyngeal muscle (0, -5, 5 % $\Delta F/F_0$). **(D)** "On-the-run"- experiment of OVC in pharyngeal muscle. **(E)** Example DVB voltage fluorescence (lower panel) and wavelength (upper panel) traces upon suppression of an AP by the OVC. Inset: Close-up and overlay of spontaneous (light gray trace) and clamped (black trace) DVB voltage signal. Monochromator wavelength is presented in the respective color. Voltage signal and movement artefact highlighted in blue and grey, respectively.

Extended data video 1. *C. elegans* expressing BiPOLES in cholinergic motor neurons, during a wavelength ramp from 400-600 nm. Animal crawling on solid substrate, with inactive (relaxed) muscle, transition to normal movement, followed by activated (contracted) muscle and respective paralysis, as indicated.

Extended data video 2: 'On the run' mode of the OVC, enabling adjusting membrane voltage during a running acquisition. Left panels, upper: Monochromator wavelength, lower: voltage fluorescence trace. Arrow keys indicated the live settings chosen by the experimenter.